SANDIA REPORT
SAND2021-14923
Printed November 2021

Sandia National Laboratories

Effective Permeability of a Nuclear Fuel Assembly

Dallin Keesling and Fred Gelbard

Prepared by
Sandia National Laboratories
Albuquerque, New Mexico
87185 and Livermore,
California 94550

Issued by Sandia National Laboratories, operated for the United States Department of Energy by National Technology & Engineering Solutions of Sandia, LLC.

Available to DOE and DOE contractors from
U.S. Department of Energy
Office of Scientific and Technical Information
P.O. Box 62
Oak Ridge, TN 37831

Telephone: (865) 576-8401
Facsimile: (865) 576-5728
E-Mail: reports@osti.gov
Online ordering: http://www.osti.gov/scitech

Available to the public from
U.S. Department of Commerce
National Technical Information Service
5301 Shawnee Rd
Alexandria, VA 22312

Telephone: (800) 553-6847
Facsimile: (703) 605-6900
E-Mail: orders@ntis.gov
Online order: https://classic.ntis.gov/help/order-methods/

ABSTRACT

This report aids in the development of models to perform characterization studies of aerosol dispersal and deposition within a spent fuel cask system. Due to the complex geometry in a spent-fuel canister, direct simulation of buoyancy-driven flow through the fuel assemblies to model aerosol deposition within the fuel canister is computationally expensive. Identification of an effective permeability as given in this work for a nuclear fuel assembly greatly simplifies the requirements for thermal hydraulic computations.

The results of computations performed using OpenFOAM® to solve the Navier-Stokes Equations for laminar flow are used to determine an effective permeability by applying Darcy's Law. The computations are validated against an analytical solution for the special case of an infinite array of pins for which the numerical and analytical solutions have excellent agreement. The effective permeability of a 17×17 PWR nuclear fuel assembly in a basket without spacer grids is numerically determined to be 1.850×10^{-6} m^2 for the range of fluid viscosities and pressure drops expected in a spent fuel storage canister. However, the flow is not uniform on the scale of multiple pins. Instead, significantly higher velocities are attained in the space between the assembly and the basket walls compared to the flow between the fuel pins within the assembly. Comparison with an analytical solution for fully developed flow through an infinite array of pins shows that the larger spacing near the basket walls results in about a 20% larger permeability compared to the analytical solution which does not include the enhanced flow in the space between the assembly and basket wall, or entrance and exit effects. A preliminary assessment of turbulence effects shows that with a k-epsilon model, significantly higher flow velocities are attained between the fuel pins within the assembly compared to the flow velocity in the space between the assembly and the basket walls. This is the opposite of what is determined for laminar flow.

ACKNOWLEDGEMENTS

OpenFOAM® software by OpenCFD Ltd, obtained from openfoam.com was used in this work.

CONTENTS

ABSTRACT 3
List of Figures 7
List of Tables 8
Acronyms and Definitions 9
1. Introduction 11
2. OpenFOAM® Model 13
   2.1. Geometry 13
   2.2. Boundary and Initial Conditions 17
   2.3. Permeability Determination 18
3. OpenFOAM® Results and Discussion 19
   3.1. Results of Test Cases 19
   3.2. Comparison to analytical solution for an infinite lattice 24
4. Discussion of Flow Assumptions 33
5. Conclusions 39
6. References 41
Appendix A. Geometric Parameters 43
Appendix B. GCI Study 44
Distribution 47

This page left blank.

List of Figures

Figure 1. Geometry of interstitial volume between fuel pins within an assembly basket. 13
Figure 2. Top-down view of interstitial flow area with one quadrant highlighted in green on the left. This quadrant was isolated as shown on the right to accelerate computational speed. 14
Figure 3. Top-down view of assembly with typical geometric nodalization. 15
Figure 4. Close-up view of nodalization around a single fuel pin. 16
Figure 5. Plot of fluid superficial velocity as a function of distance down the assembly. 16
Figure 6. Velocity contour plot for Case #1, ΔP = 5 Pa and $\mu = 4 \times 10^{-5}$ Pa*s. 20
Figure 7. Velocity contour plot for Case #2, ΔP = 5 Pa and $\mu = 2 \times 10^{-5}$ Pa*s. 21
Figure 8. Velocity contour plot for Case #3, ΔP = 10 Pa and $\mu = 4 \times 10^{-5}$ Pa*s. 22
Figure 9. Velocity contour plot for Case #4, ΔP = 10 Pa and $\mu = 2 \times 10^{-5}$ Pa*s. 23
Figure 10. Velocity distribution for 3x3 fuel assembly with uniform pin size. 26
Figure 11. Velocity distribution for 7x7 fuel assembly with uniform pin size. 27
Figure 12. Velocity distribution for 11x11 fuel assembly with uniform pin size. 28
Figure 13. Velocity distribution for 17x17 fuel assembly with uniform pin size. 29
Figure 14. Close-up of the velocity distribution of a single channel for which the boundary conditions in this small region corresponds to an infinite array of uniformly sized fuel pins. 30
Figure 15. Plot of permeability as a function of assembly size of uniform pins. 31
Figure 16. Velocity contour plot for the turbulent test case, ΔP = 10 Pa and $\mu = 2 \times 10^{-5}$ Pa*s. 37
Figure 17. Turbulent viscosity contour plot for the turbulent test case, ΔP = 10 Pa and $\mu = 2 \times 10^{-5}$ Pa*s. 38
Figure 18. Plot of permeability as a function of cell count. 45

List of Tables

Table 1. Test Matrix.....19
Table 2. Summary of results for fluid density of 0.922 kg/m^3. 24
Table 3. Tests for model validation with a constant pin diameter of 0.374 in. (9.50 mm), pressure gradient of 1.3 Pa/m and fluid dynamic viscosity of 4×10^{-5} Pa*s.....25
Table 4. Data reported by Galloway and Epstein [1965] for a 4x4 pin array with a pitch of 0.5015 inches (12.74 mm) inside a square duct with a side length of about 2 inches (50.8 mm).....34
Table 5. Reynolds number for test cases in this work with a porosity of 0.572, hydraulic diameter of 12.67 mm, and fluid density of 0.922 kg/m^3. 34
Table 6. Model Coefficients for k-epsilon turbulence model. 36
Table 7. Fuel assembly basket geometric parameters.....43
Table 8. Summary of results from GCI study.....45

Acronyms and Definitions

Abbreviation	Definition
CFD	Computational Fluid Dynamics
DOE	Department of Energy
GCI	Grid Convergence Index
MAGNASTOR®	Modular Advanced Generation Nuclear All-Purpose Storage
PWR	Pressurized Water Reactor
Re	Reynolds number
SNL	Sandia National Laboratories

This page left blank.

1. Introduction

Spent nuclear fuel is stored in sealed canisters to prevent release to the environment. In proposed designs, many fuel assemblies are stored vertically in a canister [NAC, 2010]. Pressurized helium circulates inside the canister due to natural convection driven by decay heating. In the event of a fuel rod rupture and release of radioactive aerosol particles, the helium flow will transport the particles throughout the canister. The natural flow within the canister, and the external surface area of the fuel rods, provide ample opportunity for radioactive aerosol particles to deposit on the fuel rods. The amount of aerosol deposition is dependent on several variables including the particle size distribution, temperature gradients, and the flow velocities in the canister. The objective of this work is to provide a practical method for modeling the flow in a canister with multiple assemblies, to be used with other analysis to determine aerosol deposition.

Flow modeling is computationally very intensive for even a single 17×17 pressurized water reactor (PWR) assembly, which requires meshing the interstitial space between 264 fuel pins and 25 slightly larger guide tubes. As noted by Capone [2012], "For a full core simulation of even a quarter of core simulation still today there is not enough computing power if all the spacers and mixing devices are considered through a body fitted mesh. Even the simulation of a single full-length assembly 17×17 would require several billion cells for a LES (Large Eddy Simulation) using wall functions at operational Reynolds number." Billions of cells for one assembly is impractical. Furthermore, the number of cells needed to model the flow for 37 such assemblies in a canister, with flow coupling in the open ends, combined with flow in the annular space, and including heat transfer is even more impractical.

Modeling flow through the interstitial space between fuel rods can be greatly simplified by determining the friction coefficient, or equivalently the permeability of an assembly, which is the inverse of the friction coefficient. This work analyzes the isothermal laminar flow velocity in an idealized assembly to determine the effective assembly permeability. With the permeability of an assembly, the complex details of the geometry of the interstitial space is not meshed. Instead, the assembly is modeled as a homogeneous porous medium which greatly simplifies the model but retains the effect of the flow resistance by the rods. This approach has been used to model assemblies as a porous media [Lee et al. 2009; Zigh and Gonzalez, 2017], and for flow through other complex geometries [Hooman and Gurgenci, 2010].

For the idealized case of an infinite array of uniform pins far from the inlet and outlet, an analytical solution can be obtained for laminar flow. For this problem, symmetry is used such that only a fraction of the region between several pins is analyzed and the problem is reduced to solving Laplace's Equation in two dimensions [Sparrow and Loeffler, 1959]. Tamayol and Bahrami [2010] used this approach to determine the permeability for this idealized flow in an infinite array of pins.

Actual assemblies do not consist of an infinite number of rods and have basket walls which add flow resistance. Furthermore, end effects can be important. Therefore, the porous media representation cannot be determined analytically since a finite number of pins, not all of which have the same diameter and inside a basket, no longer has the symmetry originally used by Sparrow and Loeffler [1959]. Instead, Zigh and Gonzalez [2017] developed a CFD model of an assembly to initialize the determination of the friction coefficient. Then the friction coefficient was obtained by matching the measured peak cladding temperature. They report friction coefficients in their Table 2-41 ranging from 800,000 to 1,120,000, which corresponds to permeabilities of 1.25×10^{-6} m^2 to 8.93×10^{-7} m^2, respectively.

The approach in this work is to numerically determine the permeability of an assembly for incompressible isothermal laminar flow including the basket walls and end effects. For laminar flow of a single-phase homogeneous fluid, the permeability for a nonreacting and nondeforming porous media is a property of the flow path through a porous media and is independent of the fluid properties, the forces on the fluid, and temperature. Thus, instead of modeling flow induced by thermal gradients which results in buoyancy-driven flow, a pressure gradient will be imposed. This simplifies the problem since the permeability is

independent of the forces that drive the flow. Nonetheless, the permeability determined this way can be used for problems with buoyancy-driven flow if the problem has the same geometry that was used to determine the permeability. In addition, the buoyancy-induced superficial flow velocity should be no greater than the superficial flow velocity used to determine the permeability.

The laminar flow conditions expected in the low-velocity natural circulation experienced inside the spent fuel canisters greatly reduces the computational requirements of the simulation. Compared to the estimated several billion cells required for an LES simulation of a PWR assembly during reactor operation, 26 million cells were sufficient for this idealized case. Simulations were performed using OpenFOAM® to compute the steady-state flow velocity through the assembly basket given a prescribed pressure gradient along the assembly. Once computed numerically, the steady-state superficial flow velocity is sufficient to determine the effective permeability by applying Darcy's Law as shown in Equation (1) [Bear, p. 123, 1972],

$$\vec{v} \equiv \frac{Q}{A} = -\frac{K}{\mu}\left[\nabla P - \rho\vec{g}\right], \tag{1}$$

where
$\vec{v}$ = superficial velocity vector (m/s),
Q = volumetric flow rate (m^3/s),
A = cross-sectional area including media and fluid (m^2),
K = permeability (m^2),
μ = fluid dynamic viscosity (Pa*s),
∇P = pressure gradient (Pa/m),
ρ = fluid density (kg/m^3), and
$\vec{g}$ = gravitational acceleration vector (m/s^2).

We begin in Section 2 by presenting the OpenFOAM® model and geometry. Because the assembly and basket have four-fold symmetry, only a quarter of the geometry is discretized which greatly reduces the computational effort. The boundary and initial conditions used to expedite convergence to the steady state condition is discussed. The geometric parameters for the model are given in Appendix A. Section 2 concludes with the method to determine the effective permeability from the computational results. In Section 3 the computational results are presented and discussed. Maps of the flow velocity in the interstitial region between the pins and between the basket walls and the assembly are given for four test cases. We show that for a 17×17 PWR assembly, and the range of pressure drops and fluid dynamic viscosities for a spent fuel canister, the permeability varies by less than 1%. This provides a rigorously derived value for the permeability based on the Navier-Stokes equations. However, as shown, the flow is not uniform on the scale of multiple pins. Instead significantly higher velocities are observed in the space between the basket walls and the outer pins of an assembly. To verify the accuracy of the OpenFOAM® model, comparisons are made with an analytical solution for an infinite array of uniform pins. We show that as the number of pins increases in the OpenFOAM® model, the model approaches the analytical solution. Furthermore, if symmetry conditions are used so that the OpenFOAM® model replicates the infinite array system, the OpenFOAM® model has excellent agreement with the analytical solution. Global convergence analysis is discussed in Appendix B. In Section 4 the laminar flow assumption is reevaluated. A criterion for determining the critical Reynolds number when the flow becomes turbulent is still unresolved. Finally, in Section 5 conclusions from this work are given.

2. OpenFOAM® Model

All model computations were performed using OpenFOAM®, an open-source computational fluid dynamics (CFD) package. The OpenFOAM® application utilized is simpleFoam, which implements the Semi-Implicit Method for Pressure Linked Equations (SIMPLE) algorithm to solve pressure and velocity fields using discretized momentum and mass conservation equations.

The goal of the OpenFOAM® model is to calculate the steady-state flow velocity profile of helium through a 17×17 fuel assembly basket in a dry cask storage with fluid viscosities that cover the operating temperature in the cask, which is from ambient to 400 °C, and prescribed pressure drops along the basket. These velocity profiles are then used to determine an effective assembly permeability from Equation (1). A constant fluid density of 0.922 kg/m^3 was used corresponding to the density of helium as an ideal gas at 8 atmospheres pressure and 150 °C. These are the conditions in a canister near the lower temperatures expected in a canister so that the density is high resulting in a larger Reynolds number. A discussion of the conditions for laminar flow and the Reynolds number used to determine if the flow is laminar is discussed in Section 5.

2.1. Geometry

The OpenFOAM® model geometry is shown in Figure 1. The volume considered is the interstitial space between fuel pins inside the assembly basket and the space between the assembly and the basket walls. Geometric parameters for the model are included in 0. Symmetry is used to reduce the model to a single quadrant of the assembly as shown in Figure 2. This geometric reduction greatly reduced the computational load, with negligible effect on the results.

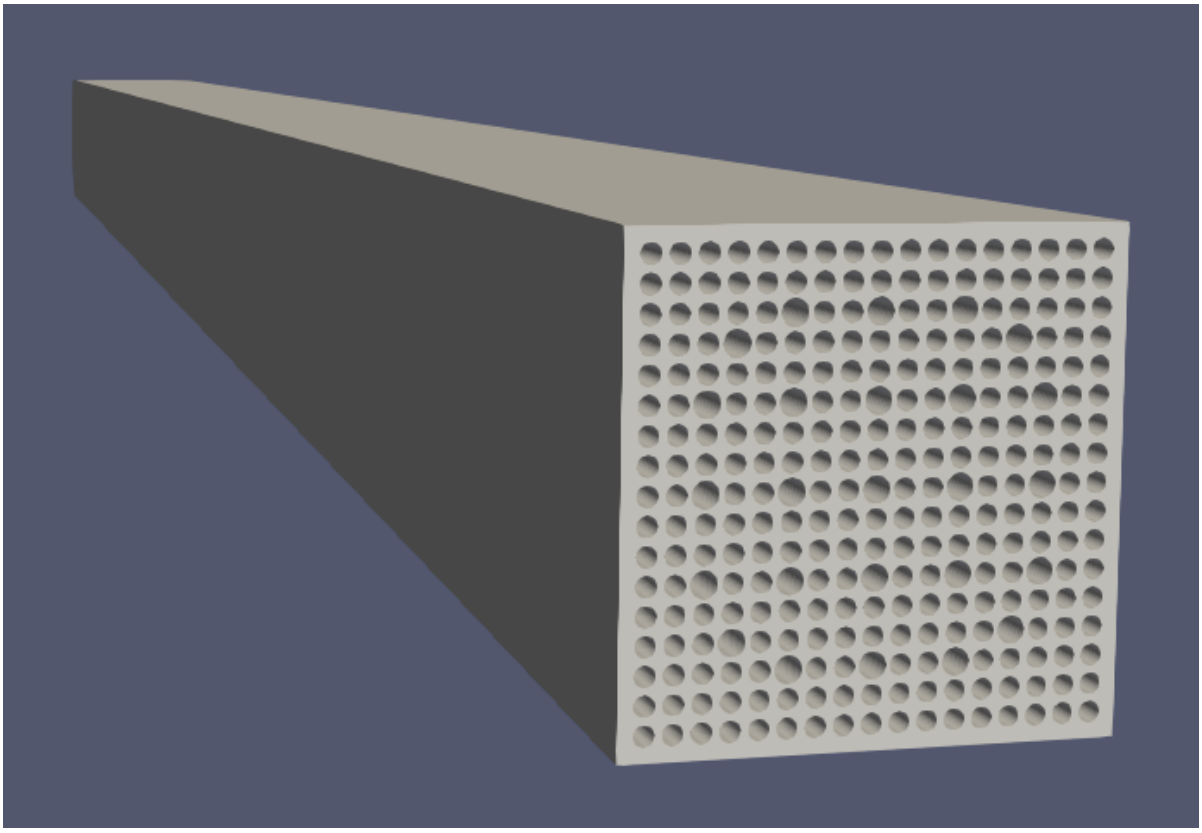

Figure 1. Geometry of interstitial volume between fuel pins within an assembly basket.

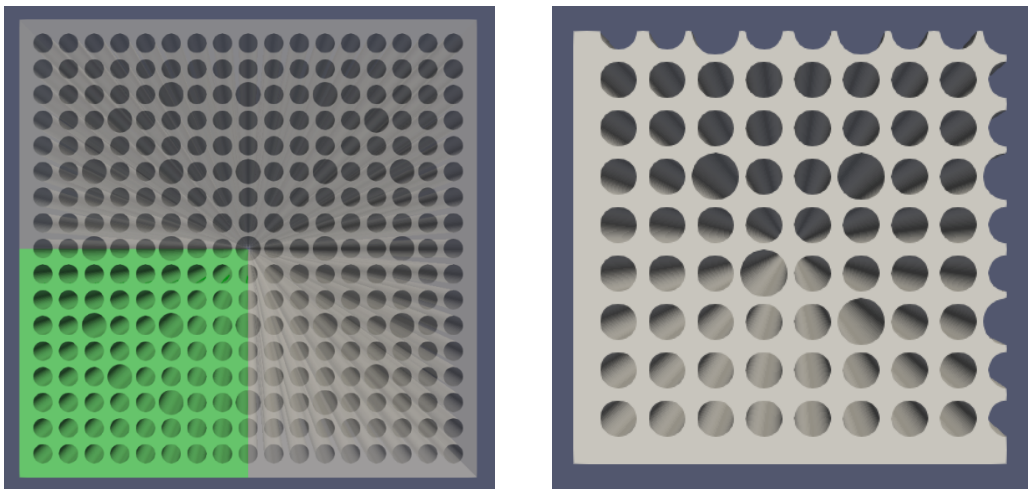

Figure 2. Top-down view of interstitial flow area with one quadrant highlighted in green on the left. This quadrant was isolated as shown on the right to accelerate computational speed.

The geometry nodalization with 30,551,040 finite volumes is illustrated in Figure 3 and **Figure 4**. Each finite volume is hexahedral in shape, with four faces parallel to the flow direction, and two perpendicular to it. Faces of some finite volumes are curved to match the curvature of nearby fuel pins. The smallest finite volumes are found close to the fuel pin walls and assembly basket walls, to capture the effects of wall friction. The mesh is more finely nodalized across the plane perpendicular to fluid flow and less finely nodalized along the length of the assembly since the flow becomes fully developed within a short distance. As shown in **Figure 5**, the flow is fully developed within the first meter of the channel, corresponding to a hydrodynamic entry length less than 5 times the width of the basket. This nodalization was determined to be sufficient by a grid convergence index (GCI) study. The study investigated three different meshes with a refinement ratio of 1.5 between them and yielded a GCI of 0.11%. The middle-refinement mesh was used for each computation in this investigation. Detailed results of the GCI can be found in **Error! Reference source not found.**.

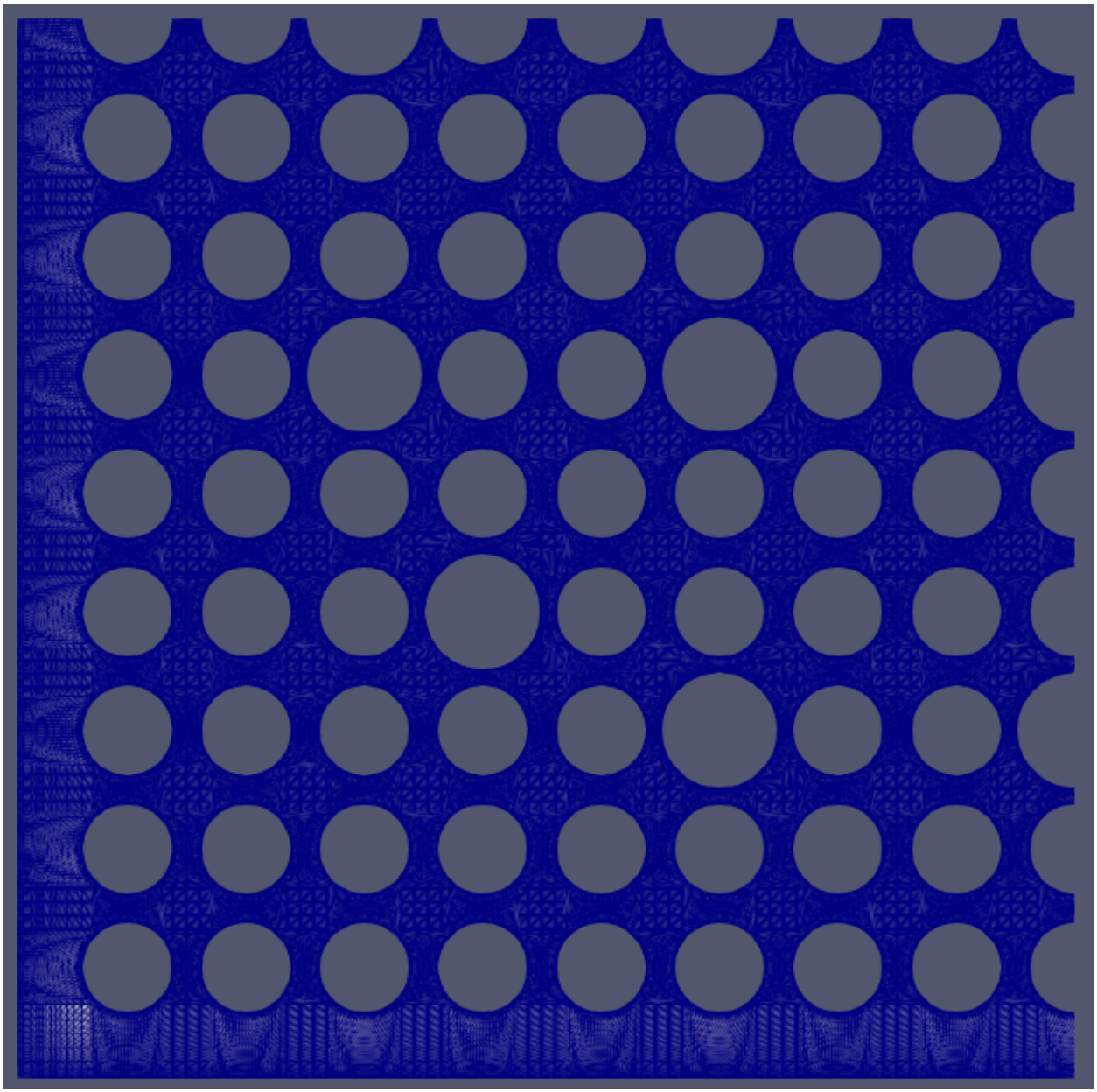

Figure 3. Top-down view of assembly with typical geometric nodalization.

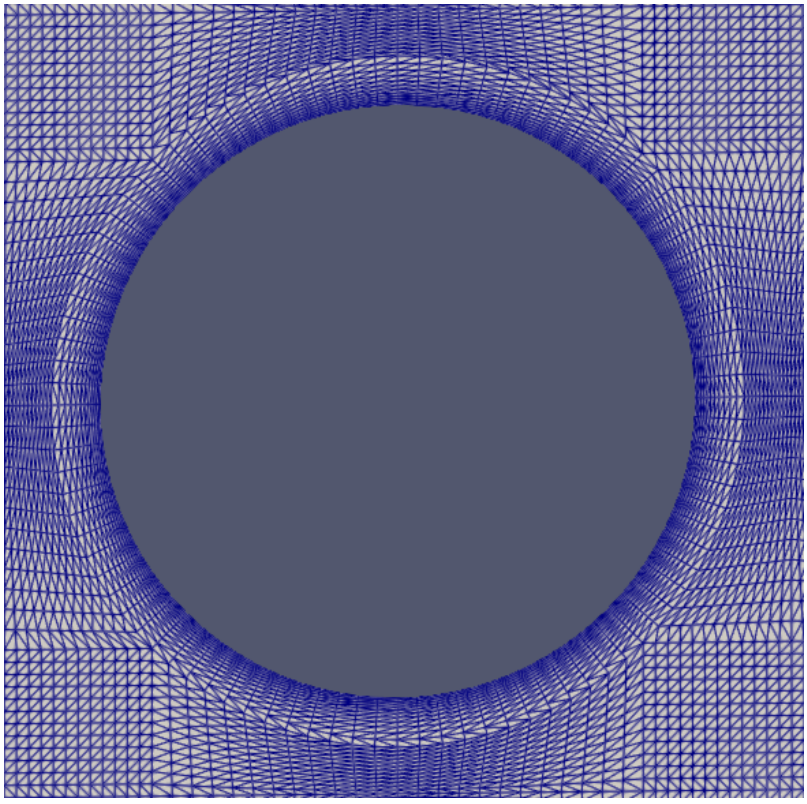

Figure 4. Close-up view of nodalization around a single fuel pin.

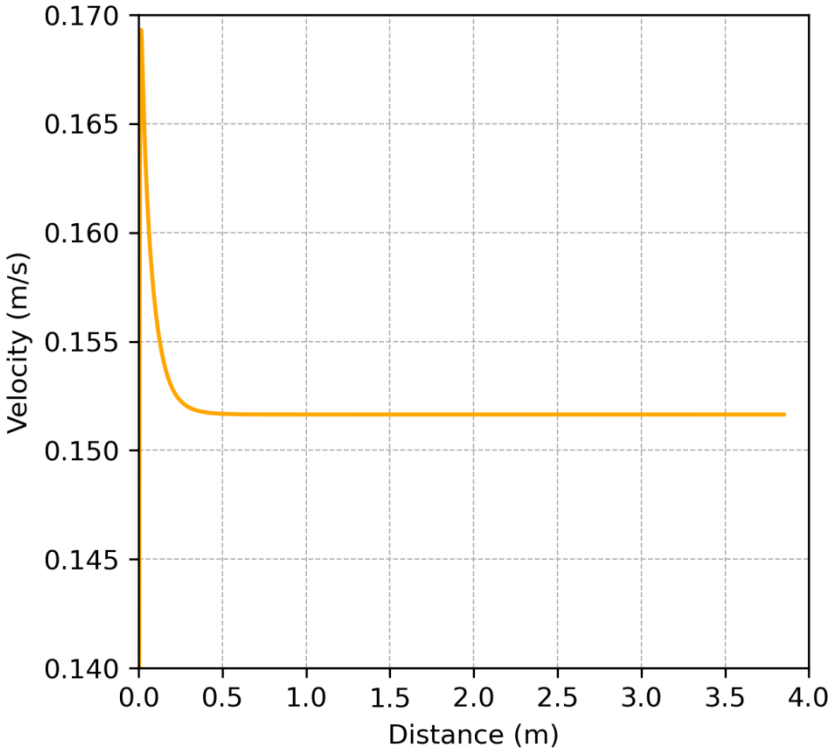

Figure 5. Plot of fluid superficial velocity as a function of distance down the assembly.

2.2. Boundary and Initial Conditions

OpenFOAM® can apply a diverse set of boundary conditions with varying levels of complexity. Some simply specify a constant value, while others affect how information is communicated from neighboring cells. Improper boundary condition application can greatly impact computation results.

Velocity boundary conditions:

- No-slip: Applied along pin walls and the outer basket wall. Velocity is held equal to zero in all directions on these walls.
- Zero Gradient: Applied at the basket outlet. The velocity is held equal to the upstream velocity.
- Pressure Inlet Uniform Velocity: Applied at the basket inlet. The uniform inflow velocity is obtained by averaging the flux over the inlet, and then applying it in the direction normal to the inlet (The OpenFOAM Foundation, n.d.). The flux is determined from the pressure gradient at the inlet.
- Symmetry: Applied along symmetry planes.

Pressure boundary conditions:

- Fixed Value: Applied at the basket inlet and outlet. Outlet pressure is set to zero, while inlet is set to prescribe the pressure drop along the assembly basket.
- Zero Gradient: Applied at pin walls and the outer basket wall. The pressure is held equal to the neighboring cell in the same z-plane.
- Symmetry: Applied along symmetry planes.

For a steady-state boundary value problem such as this one, the boundary conditions will define the end results of the computation. Initial conditions do not have a marked effect on the result, but they do influence the time required for the problem to converge. The bulk velocity is initially set to zero since the steady state velocity is expected to be low with small driving pressure differences. The initial pressure was set to approximate the expected pressure profile along the assembly basket. Since the pressure is expected to decrease linearly along the length of the basket, the pressure at a given z-position can be approximated by

$$P_z = P_{Inlet} + \left(\frac{z - z_{Inlet}}{z_{Outlet} - z_{Inlet}}\right)(P_{Outlet} - P_{Inlet}) \quad (2)$$

where
P = pressure (Pa), and
z = distance from the inlet (m).

By setting the initial pressure values approximately equal to the expected result, the time to convergence is greatly reduced.

2.3. Permeability Determination

Once the OpenFOAM® model has calculated the velocity field through the assembly basket, the effective permeability can be determined from Darcy's Law as shown in Equation (1), repeated here as,

$$\vec{v} \equiv \frac{Q}{A} = -\frac{K}{\mu}\left[\nabla P - \rho\vec{g}\right] \tag{3}$$

where
$\vec{v}$ = superficial velocity vector (m/s),
Q = volumetric flow rate (m^3/s),
A = cross-sectional area including media and fluid (m^2),
K = permeability (m^2),
μ = fluid dynamic viscosity (Pa*s),
∇P = pressure gradient (Pa/m),
ρ = fluid density (kg/m^3), and
$\vec{g}$ = gravitational acceleration vector (m/s^2).

Since fluid flow velocity is essentially unidirectional in the z-direction through the fuel assembly basket, the above expression can be simplified to consider only the z-component, which yields

$$v_z = -\frac{K}{\mu}\left[\frac{dP}{dz} - \rho g_z\right]. \tag{4}$$

Rearranging (4) gives an expression to directly estimate the effective permeability, K, as shown in Equation (5).

$$K = -\frac{\mu v_z}{\left[\frac{dP}{dz} - \rho g_z\right]}. \tag{5}$$

For this idealized case, the above expression can be further simplified by neglecting the effects of gravity and recognizing that

$$\frac{dP}{dz} = \frac{\Delta P}{\Delta z}. \tag{6}$$

Applying these two simplifications to (5) allows the direct calculation of K from Equation (7),

$$K = -\frac{\mu v_z \Delta \mathrm{z}}{\Delta P}. \tag{7}$$

By specifying the pressure drop, fluid dynamic viscosity, and assembly height for each computation, the permeability becomes entirely dependent on the z-component of the fluid superficial velocity. As shown in Equation (3), the superficial velocity is defined as the volumetric flowrate divided by the cross-sectional area of the assembly. The volumetric flowrate was computed by taking the surface integral of the z-component of the velocity along a cross-sectional slice of the assembly.

3. OpenFOAM® Results and Discussion

Four test cases were considered for this study to investigate possible effects due to changing the prescribed pressure drop along the basket or the fluid dynamic viscosity. The test matrix of cases considered are described in **Table 1**, with the computed permeabilities given later in Table 2. The two values of the viscosity correspond to the viscosity of helium in the approximate range of 300 – 800 K [Holman, 1981]. These temperatures are in the operational range of the canister of ambient to 400 °C. The pressure drop along an assembly in a canister was found to be about 2.5 Pa for a permeability of 10^{-6} m^2 [Phillips and Gelbard, 2021]. Therefore, the pressure drops used in this work as given in Table 1 were chosen to be larger since that would result in more flow but should still be laminar. Additional computations were performed to investigate the model's fidelity to established analytical solutions for laminar flow that predict the effective permeability of channels filled with regularly spaced cylinders such as found in a PWR fuel assembly basket.

Table 1. Test Matrix.

Case #	Pressure Drop, ΔP (Pa)	Dynamic Viscosity, μ (Pa*s)	Figure Number
1	5.0	4.0×10^{-5}	6
2	5.0	2.0×10^{-5}	7
3	10.0	4.0×10^{-5}	8
4	10.0	2.0×10^{-5}	9

3.1. Results of Test Cases

Contour plots of the z-component of the fluid velocity are presented in this section for each test case. These plots are cross-sectional slices of the fuel assembly 3 meters from the inlet of the channel. One common trend that is visible in all four cases is that the velocity field is not uniform throughout the flow area. In addition to local velocity differences between fuel pins due to wall effects, there is a substantial increase in velocity between the outer edge of the assembly and the basket walls. Helium flows more rapidly through this relatively large gap on the periphery. A summary of the results is given in Table 2.

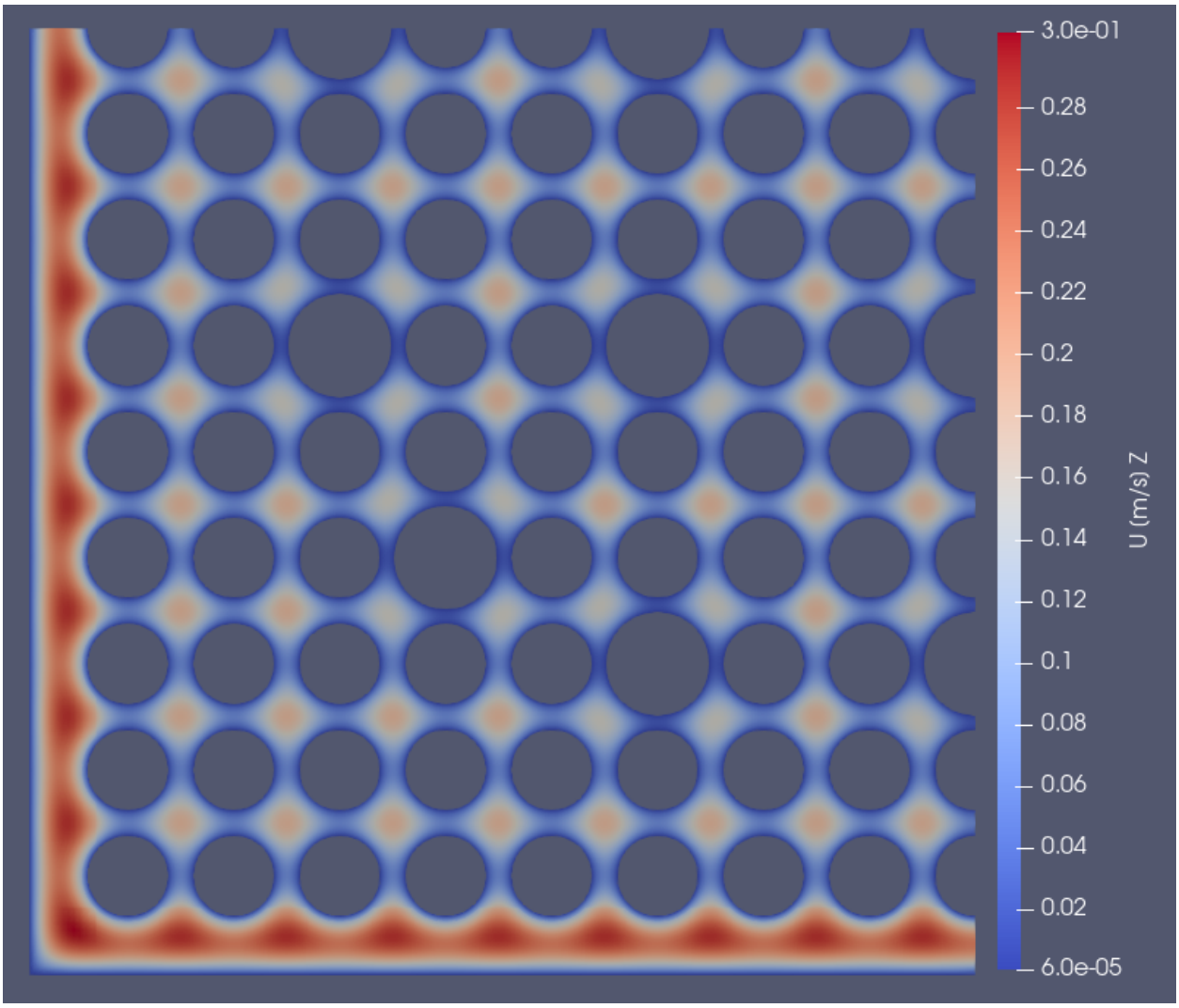

Figure 6. Velocity contour plot for Case #1, ΔP = 5 Pa and $\mu = 4 \times 10^{-5}$ Pa*s.

Case #1 resulted in the lowest superficial velocity. As shown in **Figure 6**, the maximum velocity along the outer edge is approximately 0.3 m/s. This relatively low velocity is expected since this case had both the lowest driving pressure difference and the highest fluid dynamic viscosity. The superficial velocity for case #1 is 0.060431 m/s. Applying Equation (7) yields a permeability of 1.862×10^{-6} m^2. These results are summarized below in Table 2.

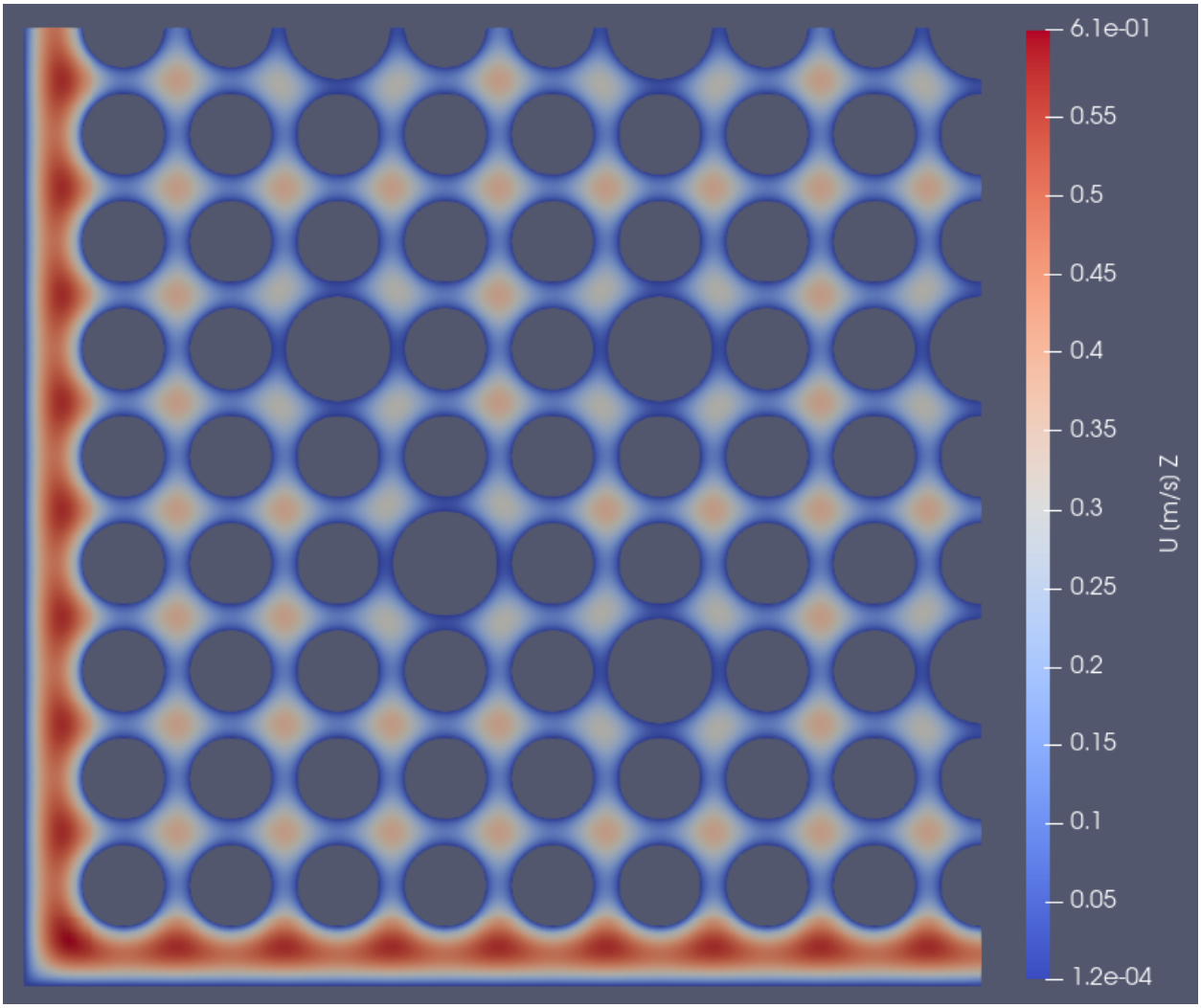

Figure 7. Velocity contour plot for Case #2, ΔP = 5 Pa and $\mu = 2 \times 10^{-5}$ Pa*s.

Halving the fluid dynamic viscosity resulted in a superficial velocity of 0.12005 m/s for case #2, approximately double that of the first case. As shown in **Figure 7**, the velocity throughout is noticeably higher than was seen in case #1, with a maximum velocity on the outer edge of approximately 0.6 m/s. Applying Equation (7) yields a permeability of 1.849×10^{-6} m^2. These results are summarized in Table 2.

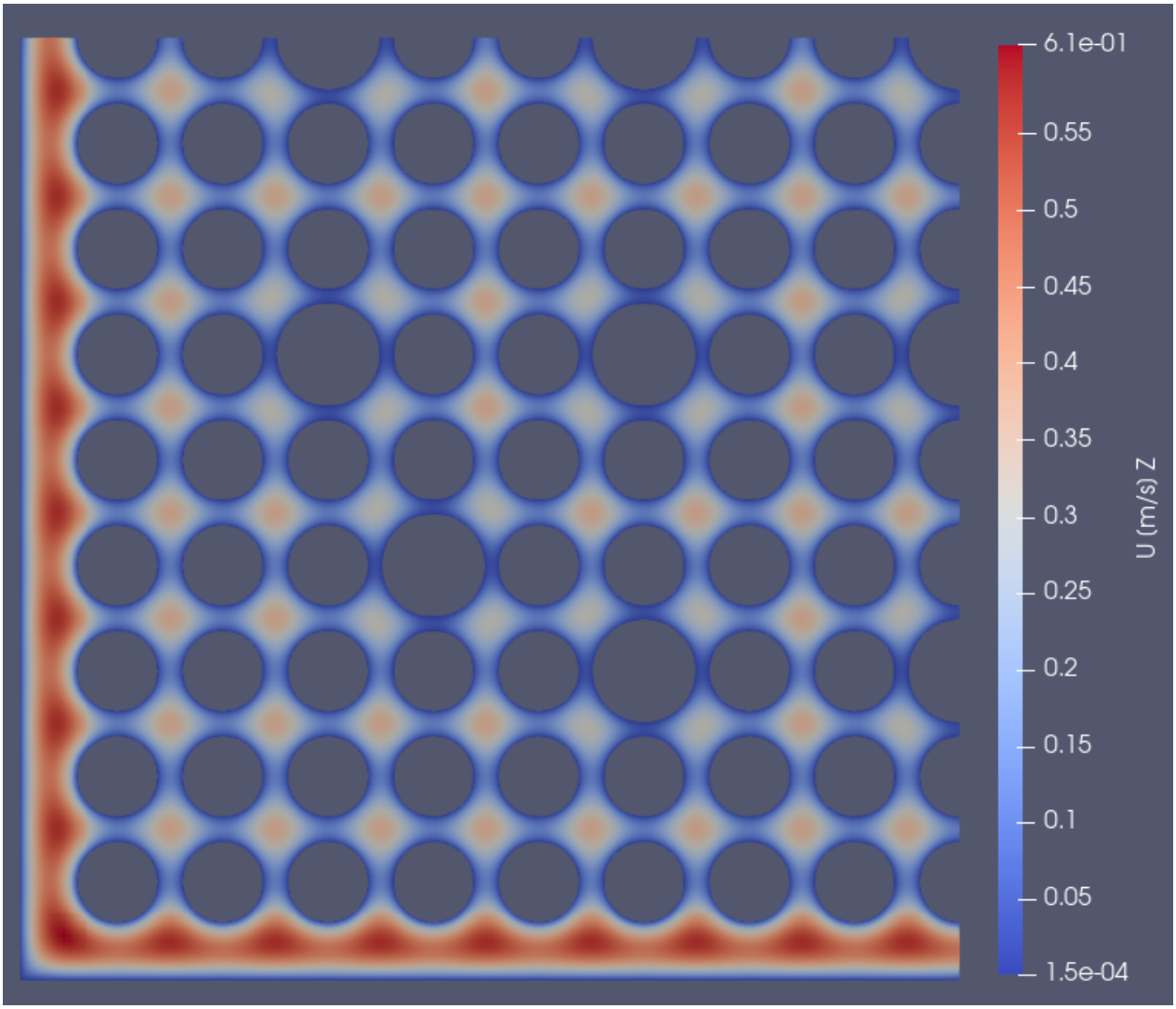

Figure 8. Velocity contour plot for Case #3, ΔP = 10 Pa and $\mu = 4 \times 10^{-5}$ Pa*s.

For case #3, the driving pressure difference was doubled to 10 Pa, and the fluid dynamic viscosity was returned to the base case. Visual comparison between **Figure 8** and **Figure 7** shows no apparent difference between the two tests, with an approximate maximum velocity of 0.6 m/s in both cases. The superficial velocity for case #3 is 0.1206 m/s, which is slightly higher than observed in case #2. Applying Equation (7) yields a permeability of 1.858×10^{-6} m^2. These results are summarized in Table 2.

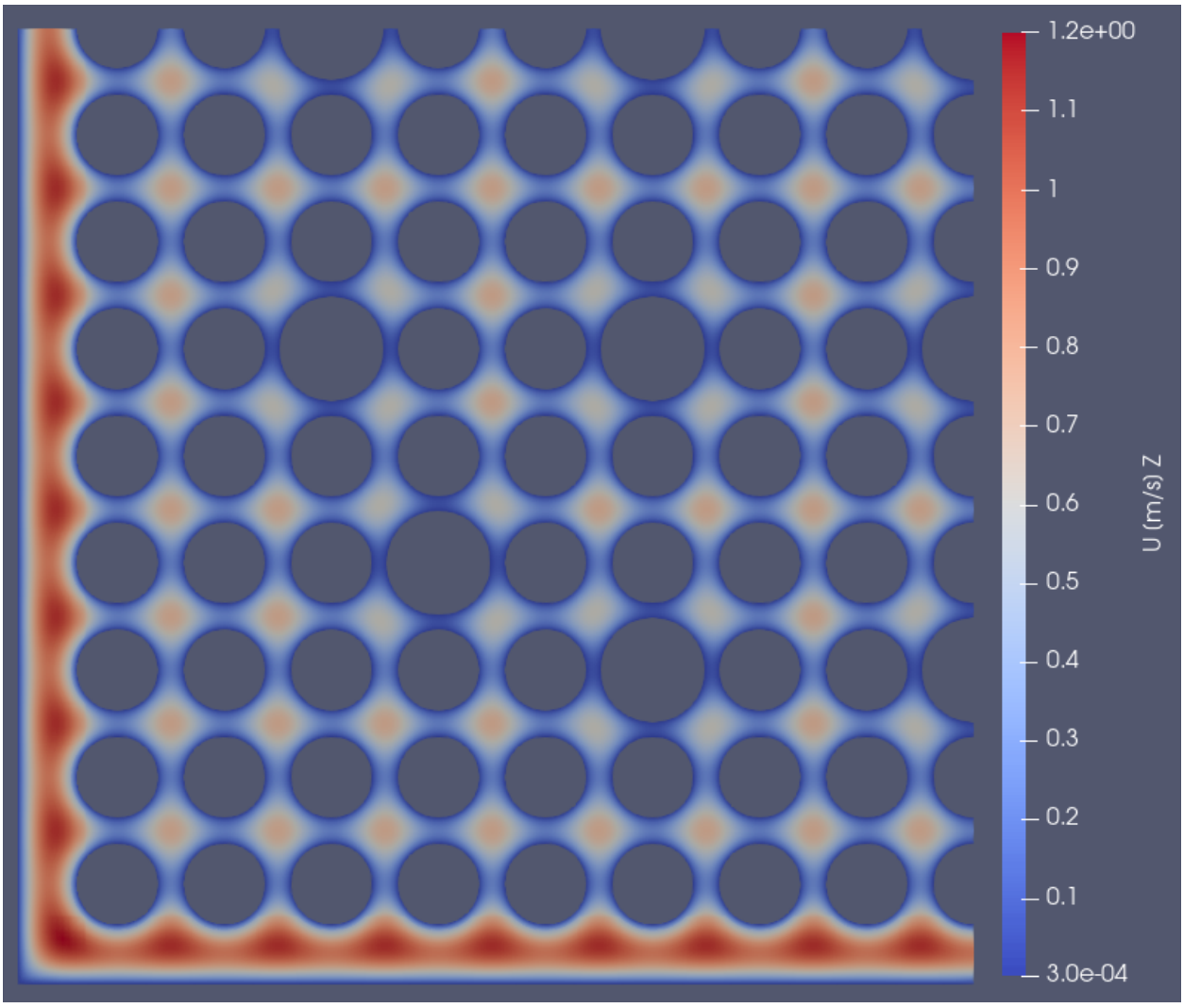

Figure 9. Velocity contour plot for Case #4, ΔP = 10 Pa and $\mu = 2 \times 10^{-5}$ Pa*s.

For the final case, a driving pressure of 10 Pa was used in combination with the lower fluid dynamic viscosity of 2×10^{-5} Pa*s. As shown in **Figure 9**, the superficial velocity is considerably higher in this case than the other cases, with a maximum velocity on the outer edge of approximately 1.2 m/s. The superficial velocity is 0.23787 m/s. Applying Equation (7) yields a permeability of 1.832×10^{-6} m^2. These results are summarized in Table 2.

Table 2. Summary of results for fluid density of 0.922 kg/m³.

Case	Pressure Drop, ΔP (Pa)	Dynamic Viscosity, μ (Pa*s)	Approximate Maximum Velocity between Assembly and Basket Walls (m/s)	Superficial Velocity, v_z (m/s)	Permeability, K (m^2)
1	5.0	4.0×10^{-5}	0.3	0.060431	1.862×10^{-6}
2	5.0	2.0×10^{-5}	0.6	0.12005	1.849×10^{-6}
3	10.0	4.0×10^{-5}	0.6	0.12061	1.858×10^{-6}
4	10.0	2.0×10^{-5}	1.2	0.23787	1.832×10^{-6}

A summary of the results from each test case is shown in Table 2. As expected, there was very little variation in the permeability result due to changes in viscosity and pressure. The mean value for the permeability is 1.850×10^{-6} m². The greatest deviation from the mean was observed for test case #4, which differs from the mean value by 0.98%. These results establish that the permeability for a PWR assembly in a basket without spacer grids is 1.85×10^{-6} m² for pressure drops up to 10 Pa and fluid viscosities of 2.0×10^{-5} Pa*s or more. These ranges cover the conditions expected in a spent fuel canister filled with helium at 8 atmospheres pressure and up to 400 °C.

3.2. Comparison to analytical solution for an infinite lattice

Tamayol and Bahrami [2010] proposed an analytical expression for steady, fully developed, laminar flow to predict the permeability through an infinite lattice of regularly sized and spaced cylinders positioned parallel to the flow direction. The correlation calculates permeability as a function of cylinder diameter, d , and media solid-fraction, ϕ in a square lattice as shown in Equation (8),

$$K = \frac{d^2}{16\phi}\left[-1.479 - \ln(\phi) + 2\phi - \frac{\phi^2}{2} - 0.0186\phi^4\right]. \quad (8)$$

ϕ is calculated as a function of cylinder diameter, d, and spacing, S, by Equation (9) with the values taken from Table 4 as,

$$\phi = \frac{\pi d^2}{4S^2} = \frac{\pi(0.374)^2}{4(0.496)^2} = 0.447. \quad (9)$$

Equation (8) provides a lower limit of the permeability through a 17×17 PWR assembly with uniformly sized pins of 0.374 in. diameter to be 1.514×10^{-6} m². This is about 20% lower than the average of the values given in Table 2. As mentioned previously, there is a substantial increase in velocity between the assembly and the inner sides of the basket as helium flows more rapidly through the relatively large gap on the periphery of the assembly. This may be why the permeability is larger for the actual geometry compared to the expression given in Equation (8).

Five more computations were performed in addition to the primary test cases described previously. The goal of these computations is to validate the OpenFOAM® model against an analytical solution which does not include end effects. Each of these computations used the same fluid parameters and boundary conditions as were used in case #1. Namely, the driving pressure was 5 Pa and the fluid viscosity was 4×10^{-5} Pa*s. A description of each test is provided in **Table 3**. For the '3×3', '7×7', '11×11', and '17×17' tests, a single quadrant of the fuel assembly is modeled, as was done in the primary computations. Unlike the geometry used in the primary computations, the geometry was simplified for these cases to use a constant pin diameter of 0.374 in. (9.50 mm) throughout the assembly. This was done to match the analytical expression shown in Equation (8), which is a function of a single pin diameter. The infinite array OpenFoam® test models flow through a single channel between four fuel pins with symmetry conditions applied at all inter-pin spaces. All OpenFOAM® tests except for the infinite array test use the same grid density as the primary computations. The infinite array OpenFOAM® test uses a higher grid density since the volume is considerably smaller, which reduced overall computational cost considerably. The agreement between the analytical solution and the OpenFOAM® solution given by the last and next to the last rows in Table 3, respectively is excellent, which validates the OpenFOAM® calculations.

Table 3. Tests for model validation with a constant pin diameter of 0.374 in. (9.50 mm), pressure gradient of 1.3 Pa/m and fluid dynamic viscosity of 4×10^{-5} Pa*s.

Test Title	Test Description	Computed Superficial Velocity (m/s)	Computed Permeability (m^2)	Figure Number
3×3	Flow through a fuel bundle with 9 elements in a square grid. 1,002,240 finite volumes.	0.1137	3.504×10^{-6}	10
7×7	Flow through a fuel bundle with 49 elements in a square grid. 4,734,720 finite volumes.	0.08399	2.587×10^{-6}	11
11×11	Flow through a fuel bundle with 121 elements in a square grid. 11,232,000 finite volumes.	0.072904	2.246×10^{-6}	12
17×17	Flow through a fuel bundle with 289 elements in a square grid. Represents the full assembly with uniform fuel pin size. 29,255,040 finite volumes.	0.0652	2.010×10^{-6}	13
OpenFOAM® Infinite array	Flow through a single channel between 4 fuel pins is modeled with symmetry conditions on all sides to represent expected results from an assembly with infinite fuel pins. 1,797,120 finite volumes.	0.04906	1.511×10^{-6}	14
Analytical Infinite array	Analytical solution given by Eq. (8) for the permeability and Eq. (4) for the superficial velocity.	0.04914	1.514×10^{-6}	

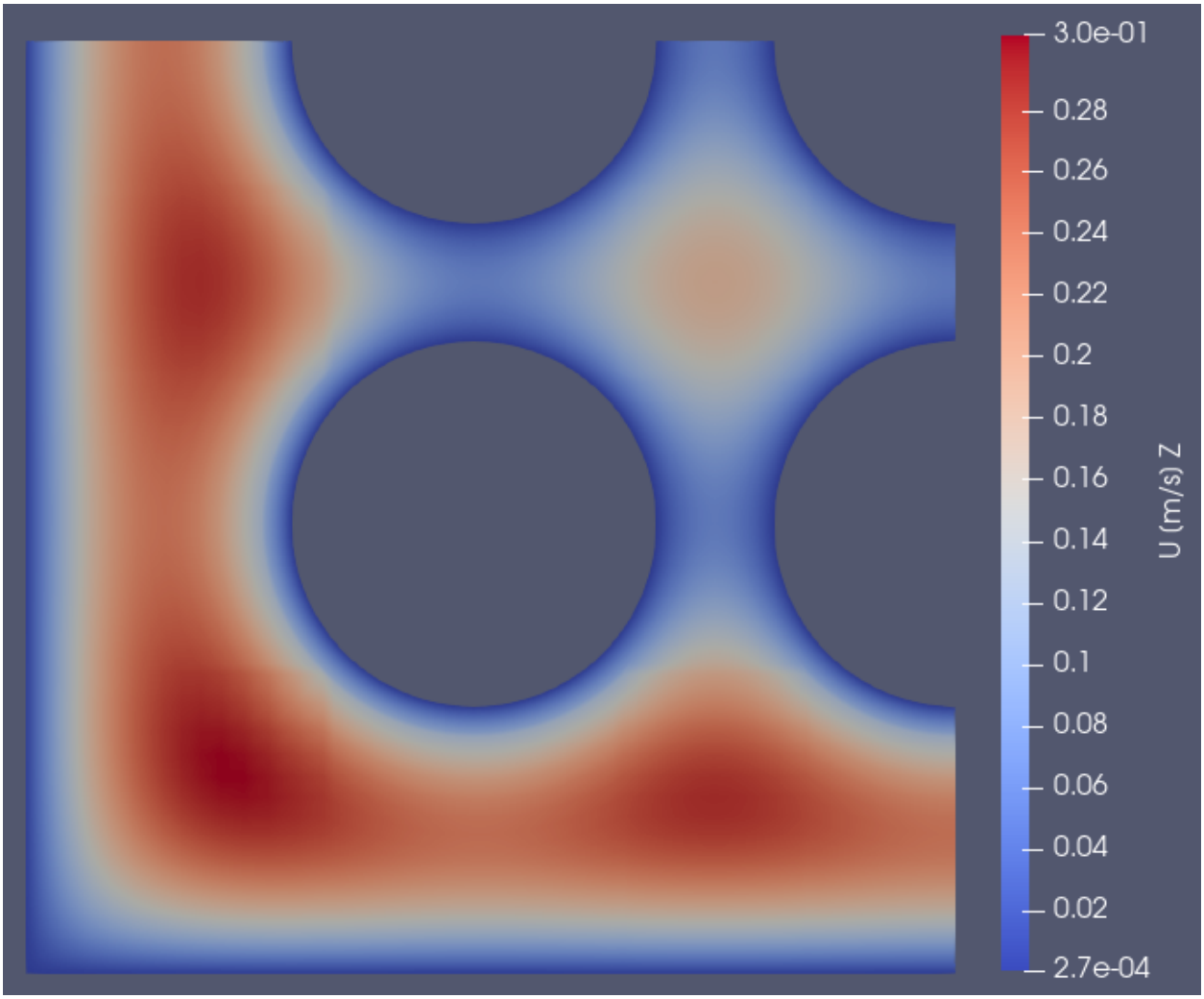

Figure 10. Velocity distribution for 3x3 fuel assembly with uniform pin size.

The velocity distribution through a theoretical 3×3 fuel assembly is shown in **Figure 10**. The highest velocity is observed to be approximately 0.3 m/s in the gap between the fuel pins and the basket walls. The superficial velocity is 0.1137 m/s, which corresponds to a permeability of 3.504×10^{-6} m^2. This is two times larger than what the analytical solution predicts for the infinite array of pins. This difference is likely due to the larger proportion of the flow that exists in the edge region. As the number of fuel pins increases, the result is expected to approach the analytical solution for the infinite array of fuel pins.

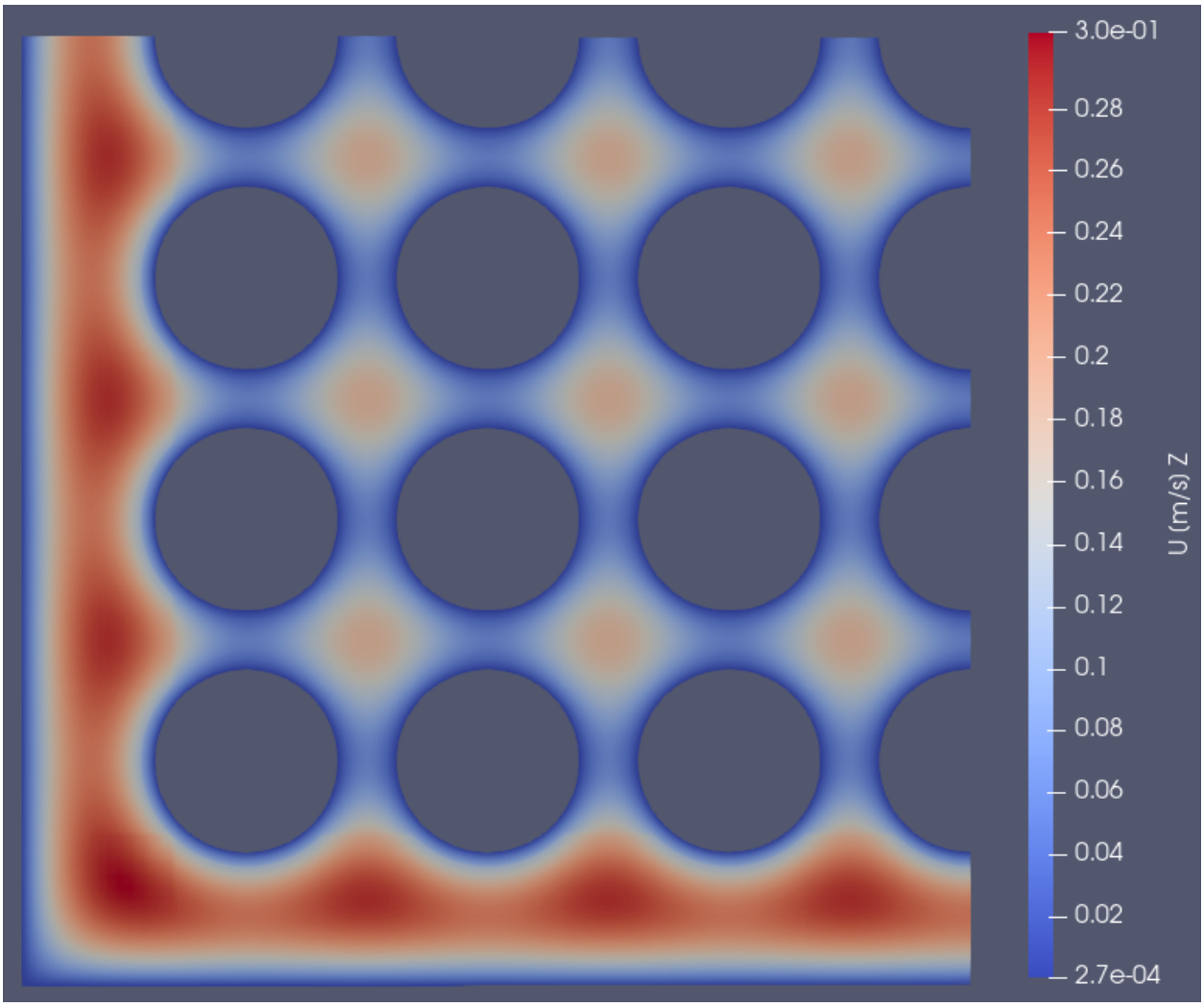

Figure 11. Velocity distribution for 7x7 fuel assembly with uniform pin size.

As shown in **Figure 11**, the velocity distribution through the 7×7 fuel assembly is similar to the 3×3 case, with a maximum velocity of approximately 0.31 m/s. Increasing the number of fuel pins also increases the proportion of the flow area that is not in the edge region, which leads to a lower superficial velocity of 0.08399 m/s. This superficial velocity corresponds to a permeability of 2.587×10^{-6} m^2.

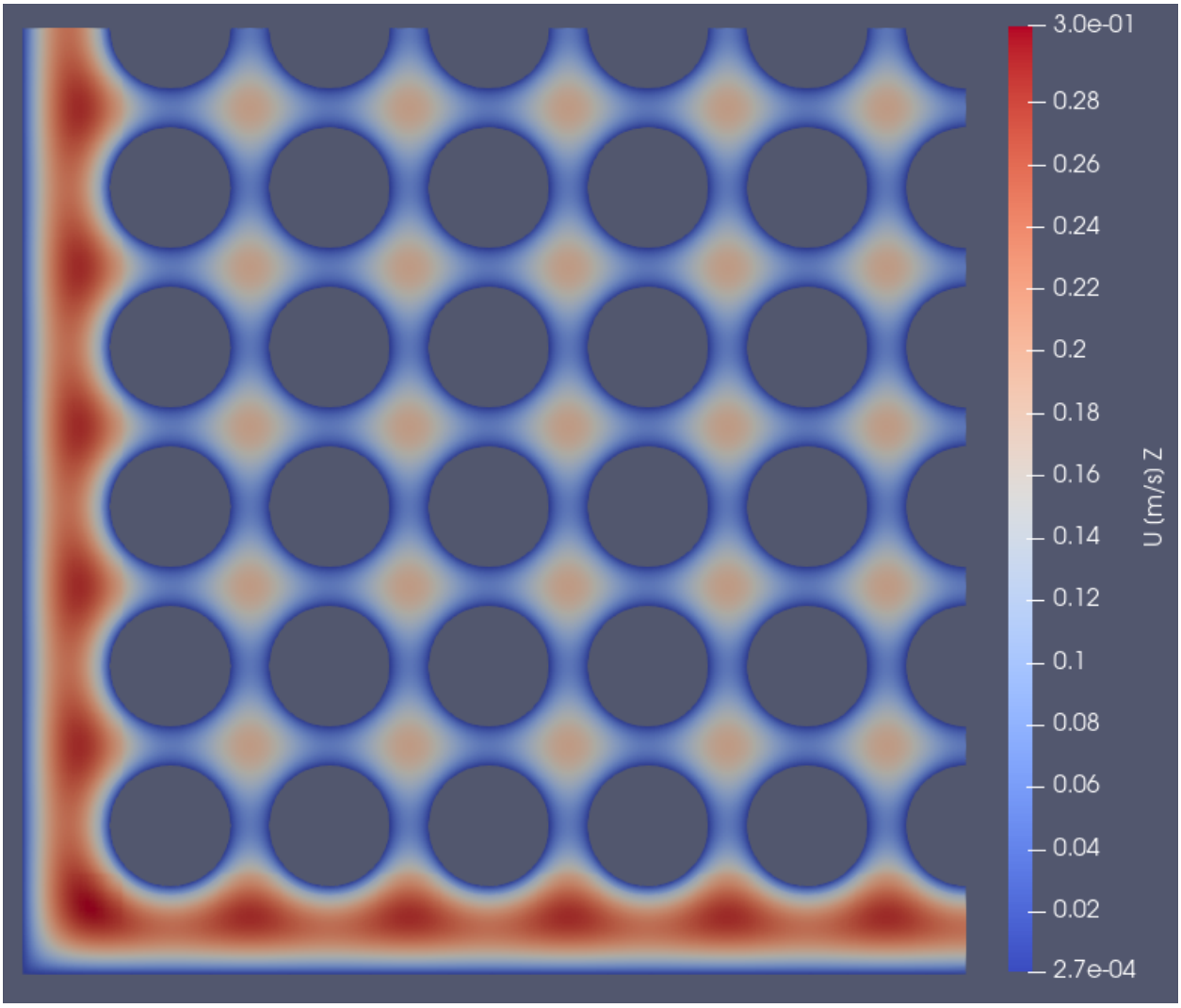

Figure 12. Velocity distribution for 11x11 fuel assembly with uniform pin size.

The superficial velocity for the 11×11 case, as shown in Figure 12, is 0.072904 m/s. This corresponds to an effective permeability of 2.246×10^{-6} m^2.

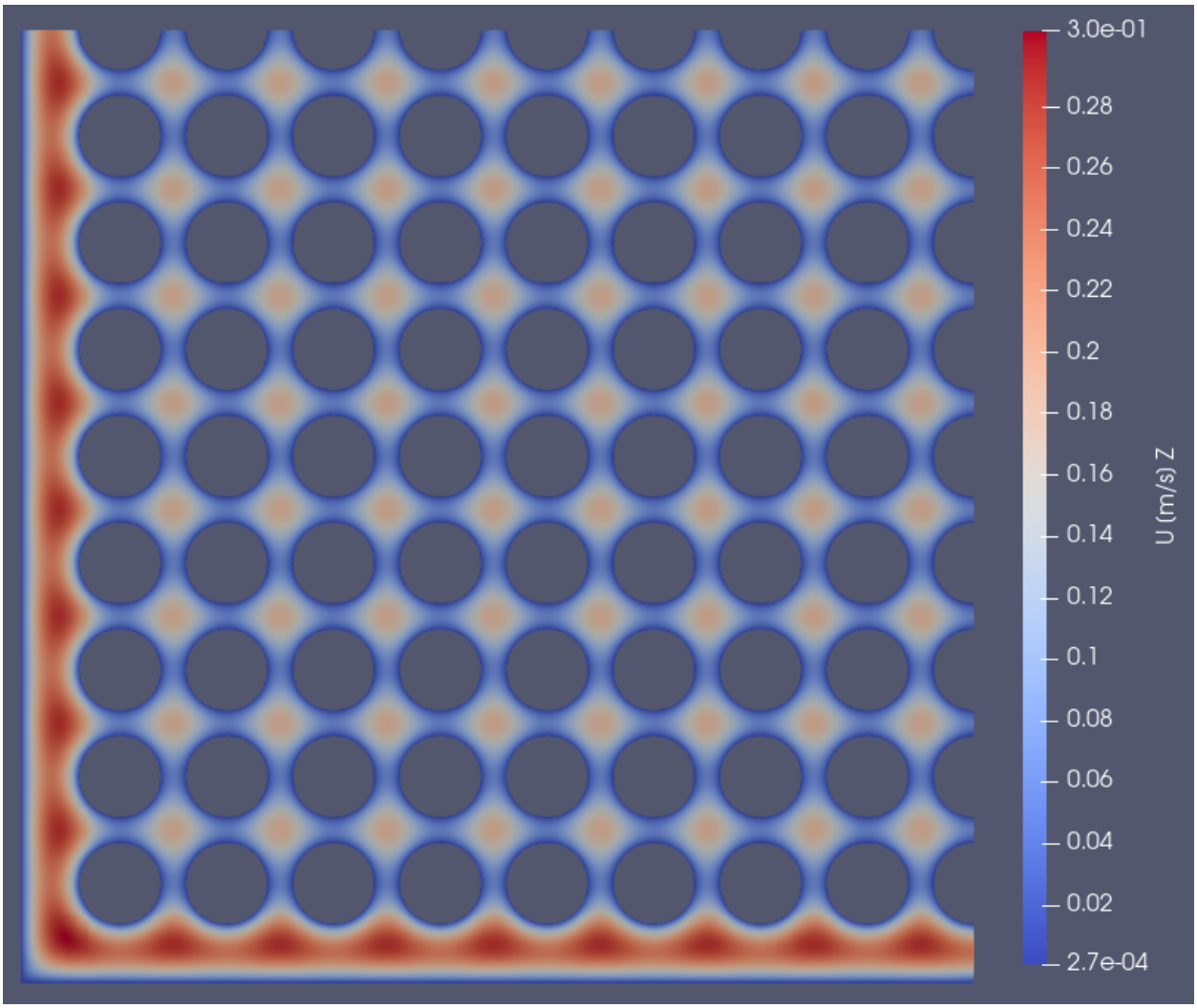

Figure 13. Velocity distribution for 17x17 fuel assembly with uniform pin size.

The velocity distribution for the 17×17 assembly is shown in **Figure 13** above. The superficial velocity is 0.0652 m/s, which corresponds to an effective permeability of 2.010×10^{-6} m^2. Comparison to the actual 17×17 assembly with some larger fuel pins shows that the uniform grid slightly over-estimates the effective permeability.

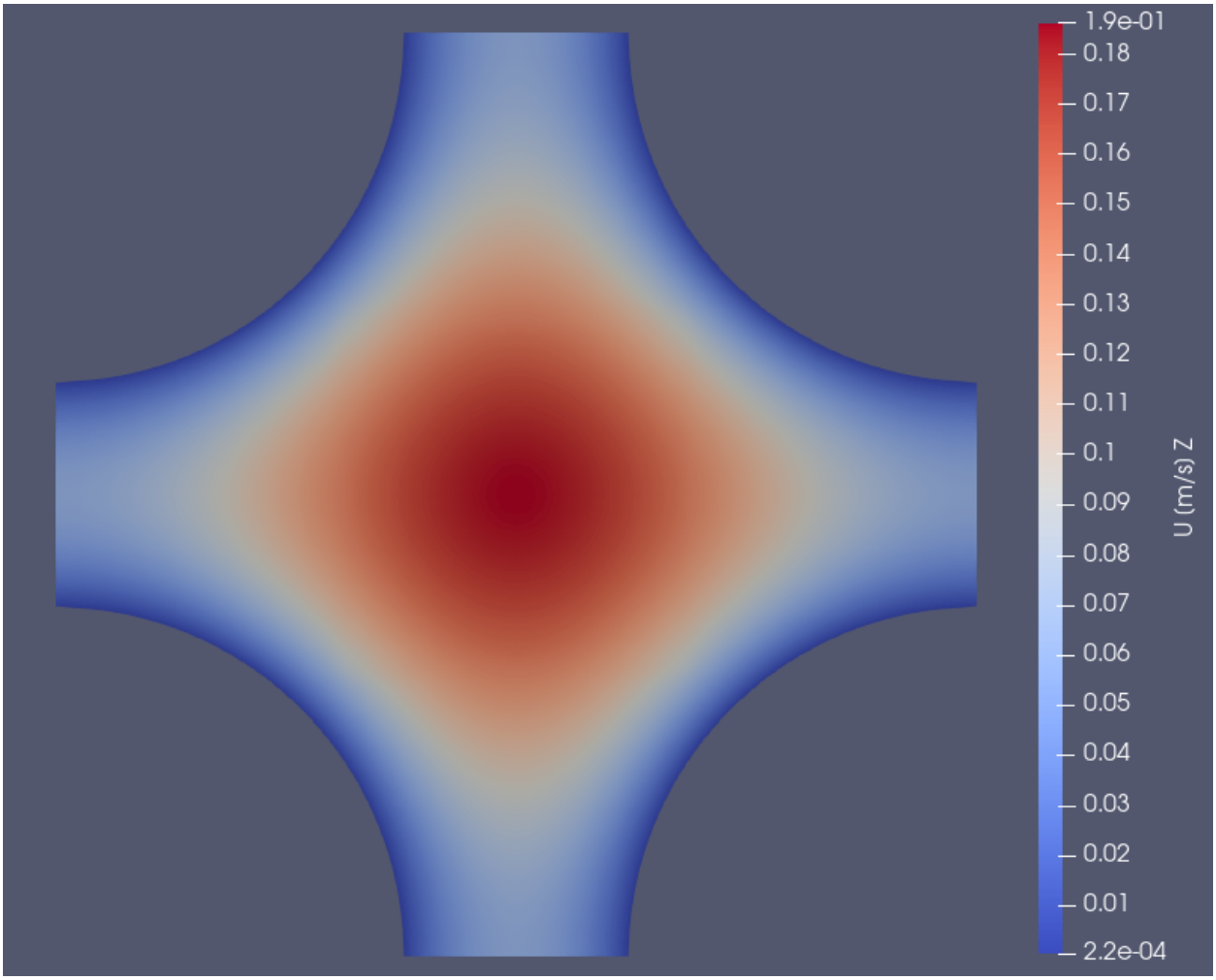

Figure 14. Close-up of the velocity distribution of a single channel for which the boundary conditions in this small region corresponds to an infinite array of uniformly sized fuel pins.

One cause for the significant difference between the effective permeabilities calculated for each of the uniform assemblies and the permeability calculated by Tamayol and Bahrami's model as shown in Equation (8) is the substantial edge region along the basket walls. These gaps along the walls lead to a higher flow rate than would be accounted for by the analytical solution. To verify the OpenFOAM® model is correctly calculating the fluid flow, an infinite array of fuel pins was modeled using a single flow channel between fuel pins and applying symmetry conditions at the inter-pin spaces. The resultant superficial velocity is 0.04906 m/s, which corresponds to 1.511×10^{-6} m^2. Comparison with the analytical result from Tamayol and Bahrami of 1.514×10^{-6} m^2 shows a deviation of less than 0.2%.

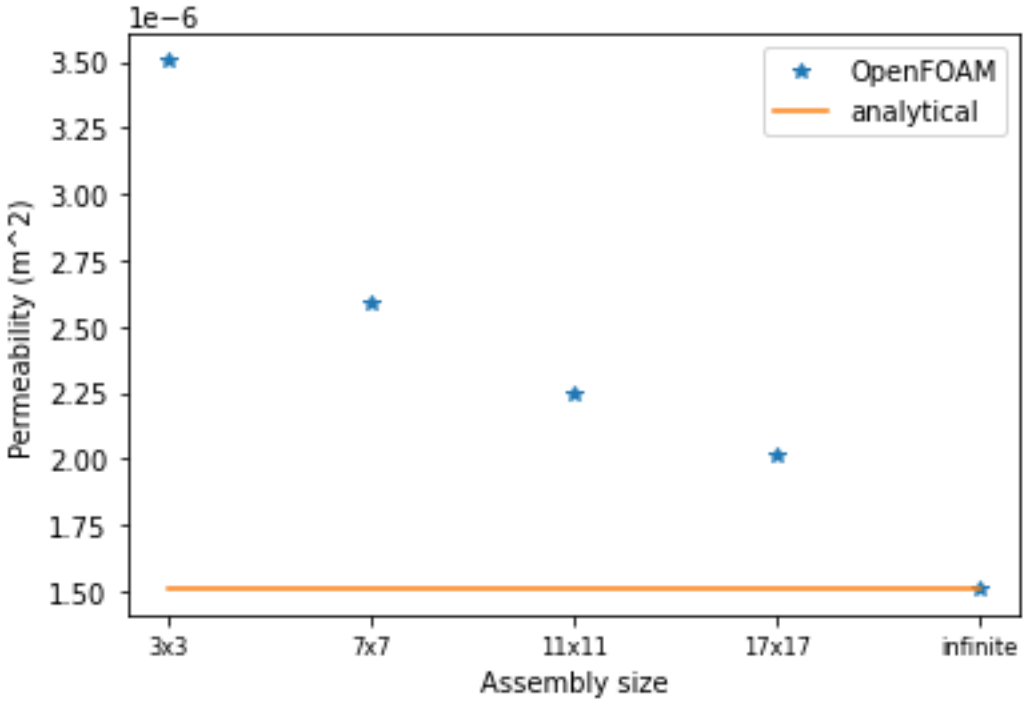

Figure 15. Plot of permeability as a function of assembly size of uniform pins.

As shown in **Figure 15**, as the size of the fuel assembly increases, the analytical solution for effective permeability of fluid flow through an array of infinite cylinders is steadily approached. By effectively modeling an infinite array in OpenFOAM directly, the analytical solution is achieved, verifying the results of the OpenFOAM model.

This page left blank

4. Discussion of Flow Assumptions

To limit computational cost, some simplifying assumptions were used to determine the flow resistance, or the inverse of the resistance which is the permeability of an assembly in a basket. The fluid was assumed to be homogenous, incompressible, and isothermal. Most importantly the level of discretization was reduced from billions of cells to millions of cells by assuming the flow resistance is uniform on a length scale no smaller than the pin spacing. If this uniformity is maintained for all pins and the flow is laminar, then a porous media representation is a valid approximation for which Darcy's Law is justified. Thus, the computations in this work showed that for laminar flow the permeability is indeed a constant independent of the pressure drop and fluid viscosity, for the ranges of these two parameters that are applicable in a spent fuel canister. This was found to be true even though the flow velocity was higher between the outer pins and the basket walls.

As noted in a classical text on porous media, [Bear, p. 126, 1972], "In practically all cases, *Darcy's law is valid as long as the Reynolds number based on average grain diameter does not exceed some value between 1 and 10*." Emphasis was not added, but the original text has this statement in italics. Extensive data that supports this statement are given in Bear [1972]. There are no grains in an assembly, so a different criterion is needed for an appropriate Reynolds number (Re) to determine if Darcy's Law is valid. Zigh and Gonzalez [page 2-1, 2017] state that "The flow regime through the assembly was modeled as laminar, as the corresponding Reynolds number based on the hydraulic diameter was below 200." Based on this statement and the problem as originally provided to the authors, the analysis in this work started with the presumption that the flow is laminar. However, we did not find data that the flow is laminar when the Reynolds number is less than 200. The validity of laminar flow based on the hydraulic diameter for the pressure drops and fluid viscosities as used in the work is now reevaluated.

The hydraulic diameter is a common length scale for flow through non-circular ducts and is defined as four times the area for flow divided by the wetted perimeter [Holman, 1981, p. 232]. For circular ducts, the hydraulic diameter conveniently reduces to the duct diameter. But as noted by Bird et al. [2007, p. 183], this length scale is for turbulent flow and is "less satisfactory" for laminar flow. Nonetheless, the hydraulic diameter provides a convenient characteristic length scale that has been used for flow through an assembly of rods in a square duct.

Galloway and Epstein [1965] performed extensive measurements on a 4×4 square array of rods in a square duct with a side length of about 2 inches. The rods were 12 feet long. The pitch, which is the distance between the centers of adjacent pins in a direction parallel to a duct wall was 0.5015 inches. For rods closest to the duct wall, the distance from the rod center to the wall was half the pitch. They varied the rod diameter while maintaining the pitch and varied the flow velocity in their experiments. The hydraulic diameter which includes the perimeter of the duct and that of the rods was used to determine the characteristic length for the Reynolds number. As given below in Table 4, the critical Reynolds number for transitioning from laminar to turbulent flow based on their measurements varied from 93 to 270 using the bulk velocity which is the superficial velocity divided by the porosity. If the critical Reynolds number was about the same for all for four rod diameters given in Table 4, then that would establish a criterion for determining if the flow is laminar or turbulent for a 4×4 assembly in a square duct. However, the critical Re in the experiments varied by about a factor of three with no clear centering on a single value. This indicates that the hydraulic diameter may not be the appropriate length scale for the Reynolds number to determine if the flow through an assembly inside a basket is laminar or turbulent. Furthermore, other parameter values may be needed to determine when the flow is laminar for a PWR assembly.

In this work for the four test cases, the fluid viscosity and pressure drop were varied, and the hydraulic diameter was constant. The bulk velocity and Reynolds number are given in Table 5 for the four test cases. In this work the hydraulic diameter of 12.67 mm and pin diameter of 9.50 mm (given in Appendix

A), fall between the second and third row, and between the third and fourth row, respectively in Table 4. For test cases 1 and 3 in Table 5, which have the higher viscosity, the Reynolds number is lower than the four critical Reynolds numbers given in Table 4. This comparison tends to support using a laminar flow model. However, this is not strong evidence that the flow is laminar even for test cases 1 and 3, because the data from Galloway and Epstein were for a 4×4 pin assembly whereas the test cases in this work were for a 17×17 assembly. Furthermore, laminar flow was assumed for calculating the velocities in Table 5. Using results that start with a laminar flow assumption to check if the flow is laminar is a necessary consistency check and not a proof. Thus, additional validation is needed that the flow is laminar in a PWR 17×17 assembly for the fluid properties and flow conditions expected in a spent fuel canister.

Table 4. Data reported by Galloway and Epstein [1965] for a 4x4 pin array with a pitch of 0.5015 inches (12.74 mm) inside a square duct with a side length of about 2 inches (50.8 mm).

Rod Diameter (in/mm)	Pitch/Rod Diameter	Hydraulic Diameter (in/mm)	Critical Re for transitioning between laminar and turbulent flow based on hydraulic diameter and bulk velocity
0.4672/11.87	1.073	0.1646/4.181	270
0.4077/10.36	1.230	0.2735/6.947	93
0.3418/8.682	1.467	0.4080/10.36	100
0.2512/6.380	1.996	0.6286/15.97	130

Table 5. Reynolds number for test cases in this work with a porosity of 0.572, hydraulic diameter of 12.67 mm, and fluid density of 0.922 kg/m^3.

Case	Pressure Drop, ΔP (Pa)	Dynamic Viscosity, μ (Pa*s)	Superficial Velocity, v_z (m/s)	Bulk Velocity (m/s)	Reynolds number based on hydraulic diameter and bulk velocity
1	5.0	4.0×10^{-5}	0.060431	0.1056	30.8
2	5.0	2.0×10^{-5}	0.12005	0.2099	123
3	10.0	4.0×10^{-5}	0.12061	0.2109	61.6
4	10.0	2.0×10^{-5}	0.23787	0.4159	243

The problem of selecting an appropriate characteristic length scale for determining a critical Re is recognized in the literature and other length scales have been proposed. Tamayol and Bahrami [2009] proposed the length scale may be based on the square root of the flow area. Another proposed length scale is the square root of the permeability [Hooman and Gurgenci 2010]. With three possible length scales, and each giving different results, data and analysis for a characteristic length scale to determine the critical Re is clearly needed.

To numerically evaluate the validity of the laminar flow assumption, the calculation was repeated for a single case with an activated turbulence model. A simple k-epsilon model, which is commonly used for flow through ducts, was used for this calculation. The k-epsilon model is a Reynolds Averaged

Simulation (RAS) model which solves two additional equations along with the Navier-Stokes equation. These are the turbulent kinetic energy equation, and the turbulent energy dissipation rate equation, shown in Equations (10) and (11) respectively

$$\frac{D}{Dt}(\rho k) = \nabla \cdot (\rho D_k \nabla_k) + P - \rho\epsilon \tag{10}$$

$$\frac{D}{Dt}(\rho \epsilon) = \nabla \cdot (\rho D_\epsilon \nabla_\epsilon + \frac{C_1 \epsilon}{k}\left(P + C_3 \frac{2}{3} k \nabla \cdot u\right) - C_2 \rho \frac{\epsilon^2}{k} \tag{11}$$

where:
k = Turbulent kinetic energy (m^2/s^2),
ϵ = Turbulent kinetic energy dissipation rate (m^2/s^3),
P = Turbulent kinetic energy production rate (m^2/s^3),
ρ = Density of the fluid (kg/m^3),
D_ϵ = Effective diffusivity for ϵ,
D_k = Effective diffusivity for k,
C_1 = Model coefficient, and
C_2 = Model coefficient.

The effective diffusivities of k and ϵ are determined as a function of the turbulent viscosity, fluid viscosity, and a model coefficient σ as shown in Equation (12).

$$D_i = \frac{\nu_t}{\sigma_i} + \nu_{fluid} \text{ for } i = k,\epsilon. \tag{12}$$

Once the values of k and ϵ are determined, they are used to calculate the turbulent viscosity by Equation (13)

$$\nu_t = C_\mu \frac{k^2}{\epsilon} \tag{13}$$

where:
C_μ = Model coefficient for the turbulent viscosity, and
ν_t = Turbulent viscosity (m^2/s).

The turbulent viscosity is then used in the Navier-Stokes equation to compute the fluid velocity, thereby estimating the effects of turbulence on the bulk motion of the fluid without resolving eddies in the flow, which is considerably more computationally expensive. The additional viscous effect due to turbulence leads to lower velocities than would be expected in a laminar regime. See **Table 6** for the model coefficients used for k-epsilon calculations in this work. These coefficients are commonly used for turbulent flows and were determined by fitting k-epsilon results to a wide range of turbulent flows (Launder & Spalding, 1974, pp. 268-289).

Table 6. Model Coefficients for k-epsilon turbulence model.

Model Coefficient	Value
C_μ	0.09
C_1	1.44
C_2	1.92
σ_k	1
σ_ϵ	1.3

For this test case, the inlet flow was assumed to have a small amount of turbulence (5% turbulent intensity) associated with helium mixing as it reaches the bottom of the spent fuel cask and begins to rise through the fuel pins. To best evaluate the laminar flow assumption for the range of conditions present in the fuel cask, a pressure drop of 10 Pa and fluid viscosity of 2×10^{-5} Pa*s were used, since they lead to the highest velocity we would expect in the flow channel. The resultant velocity contour plot is shown in **Figure 16**. The superficial velocity is 0.0113 m/s. Applying Eq. (7) yields a permeability of 8.710×10^{-8} m^2, which is much lower than was calculated under the laminar flow assumption. Since this result is presumably dependent on the degree of turbulence present in the flow, this result could not be used to represent the flow geometry across the entire range of conditions expected in a spent fuel cask.

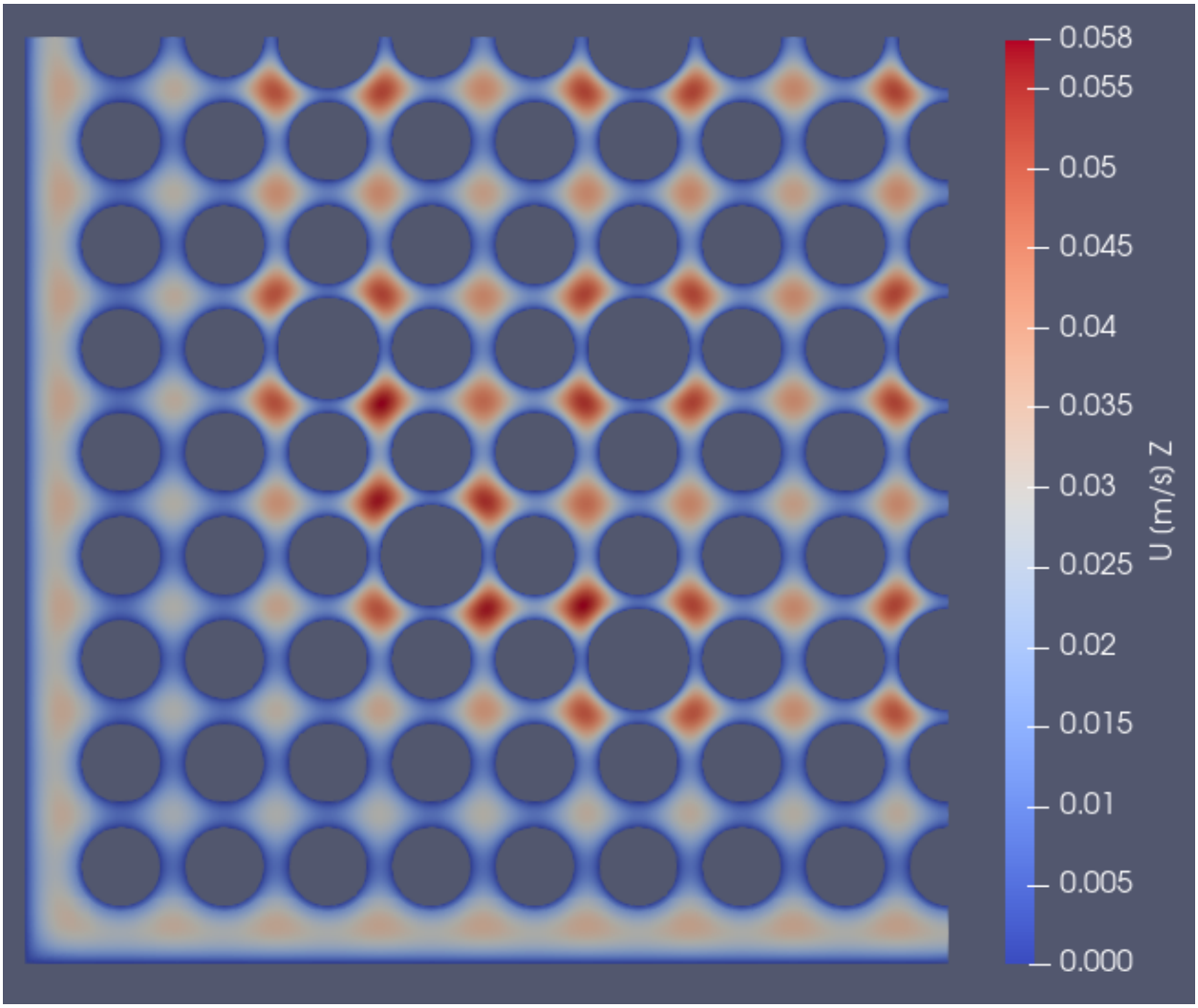

Figure 16. Velocity contour plot for the turbulent test case, ΔP = 10 Pa and $\mu = 2 \times 10^{-5}$ Pa*s.

Comparison between the results using the turbulence model and the laminar model shows a significant difference. While the highest velocity in the laminar cases was found along the outer edge of the basket due to the larger flow area, the highest velocities in the turbulent case are found amid the fuel pins, particularly in the smaller flow channels. One explanation for this difference can be seen in Figure 17, which shows a contour plot of the turbulent viscosity for the turbulent case. As shown, the turbulent viscosity is much higher in the outer regions of the flow channel where the flow area is larger. This is to be expected, since a larger flow area results in a larger Reynolds number, or increased turbulence. The maximum turbulent viscosity observed is approximately 8×10^{-4} m^2/s. Converting this to units of Pa*s by multiplying by the fluid density, 0.922 kg/m^3, yields a turbulent viscosity equal to 7.38×10^{-4} Pa*s, which is over thirty times higher than the fluid viscosity.

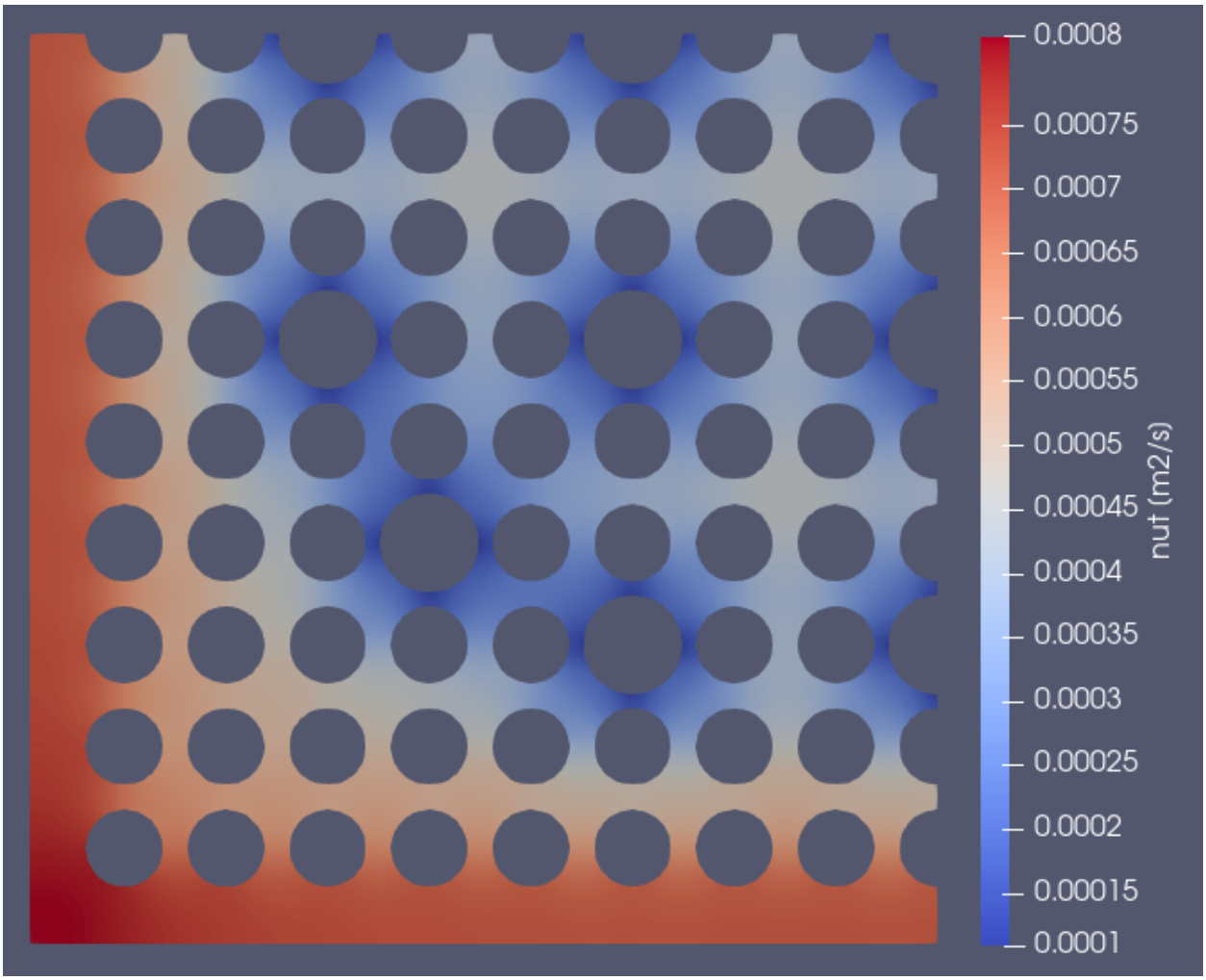

Figure 17. Turbulent viscosity contour plot for the turbulent test case, ΔP = 10 Pa and $\mu = 2 \times 10^{-5}$ Pa*s.

If Eq. (7) is adjusted to use the average effective viscosity in place of the fluid viscosity, the resultant permeability for the turbulent case is 2.015×10^{-6} m^2, which only deviates from the laminar result by 8.9%. However, given that a full numerical analysis is required to determine the average effective viscosity in a turbulent regime, it would be impractical to attempt to use Darcy's law to approximate the behavior of turbulent flow through the channel in this manner. Additionally, the use of Darcy's law would neglect the effect of turbulence on the velocity distribution.

5. Conclusions

Determining flow velocities inside a spent fuel canister due to buoyancy-driven flow is a very difficult problem due to, (1) the complex geometry of the interstitial region between fuel rods, (2) the nonuniform space between the assemblies and basket walls, (3) multiple assemblies, (4) flow obstructions such as the spacer grids, (5) coupling between assemblies in the canister headspace and base, (6) heat transfer between structures within the canister, and (7) heat transfer from the canister walls to the environment. Because of these complexities, a simpler porous media representation of the assemblies has been reported in the literature. Porous media permeability has been extensively studied for fluid flow through geological media. The media permeability can be determined for a fixed geometry using Darcy's Law for laminar flow if the flow path, fluid density, viscosity, pressure gradient, and the superficial velocity are measured or calculated. In this work the flow in the interstitial region between the rods of a PWR 17×17 assembly in a basket was modeled using OpenFOAM® to solve the Navier-Stokes Equations for laminar flow. The permeability was determined to be 1.850×10^{-6} m^2 if the pressure drop along the assembly is no larger than as used in this work of 10 Pa, and the fluid viscosity is no less than 4.0×10^{-5} Pa*s. This covers the range of these variables expected in a spent fuel canister.

Using a bulk porous media model implies that the flow is uniform on length scales much larger than the spacing between the rods. In the limit of an infinite array of pins, the flow is uniform on this length scale. A PWR assembly with 289 pins does approach the infinite array limit within 20% for the permeability. However, the flow is not uniform for a PWR assembly in a basket. For laminar flow the computations show that there is a significantly higher flow velocity between the basket walls and the outer pins of an assembly compared to the velocity between adjacent pins in the interior of the assembly. The numerical OpenFOAM® model that shows this phenomenon was verified by replicating the conditions for an infinite array by using symmetry boundary conditions. The numerical results have excellent agreement with the analytical solution for this limiting case.

Darcy's Law relies on the assumption that the flow is laminar, which may be justified if the Reynolds number is less than a critical Reynolds number. However, we found no data for the critical Reynolds number for flow through a PWR 17×17 assembly in a basket. There are also multiple proposed characteristic lengths to use for the Reynolds number for flow through an array of pins in a duct. The data by Galloway and Epstein [1965] for a 4×4 assembly do not support even an approximate single value for the critical Reynolds number based on the hydraulic diameter length scale. Further work is needed to determine the appropriate length scale and the effects of nonuniformities in the flow such as spacer grids. In addition, turbulence can significantly affect the flow and result in higher velocities between adjacent pins in the interior of an assembly compared to the region between the assembly and basket walls. This is the opposite of what is observed for laminar flow. Further analysis is needed clarify the conditions when and where laminar or turbulent flow occurs in an assembly in a spent fuel canister.

This page left blank.

6. References

Bear, J. (1972). Dynamics of Fluids in Porous Media, Dover.

Bird, R. B., W. E. Stewart, and E. N. Lightfoot (2007). Transport Phenomena, Revised second edition.

Capone, L. (2012). "CFD Analysis of Nuclear Fuel Bundles and Spacer Grids for PWR Reactors," *Doctoral dissertation, Texas A&M University. Available electronically from https://hdl.handle.net/1969 .1/ETD-TAMU-2012-08-11404.*

Galloway, L. R. and N. Epstein (1965). "Longitudinal Flow Between Cylinders in Square and Triangular Arrays and in a Tube with a Square-edged Entrances," *American Institute of Chemical Engineering Journal*, *Chemical Engineering Symposium Series*, Volume B, 4-15.

Holman, J. P, (1981). *Heat transfer*, McGraw-Hill.

Hooman, K. and Gurgenci (2010). "Porous Medium Modeling of Air-Cooled Condensers," *Transport in Porous Media* **84** (2) 257-273.

Launder, B. E. and D. B. Spalding (1974). "The Numerical Computation of Turbulent Flows," *Computer Methods in Applied Mechanics and Engineering* **3** (2) 269-289. doi:https://doi.org/10.1016/0045-7825(74)90029-2.

Lee, J. C. (2009). "Thermal-Fluid Flow Analysis and Demonstration of a Spent Fuel Storage System," *Nuclear Engineering Design* **239**, 551-558.

NAC International (2010), "MAGNASTOR® (Modular Advanced Generation Nuclear All-Purpose STORage), Final Safety Analysis Report," *August 2010 Revision 10 B, Docket No. 72-1031, Norcross, Georgia, www.nacintl.com*.

Phillips, J. and F. Gelbard (2021). "*Interim Report on Aerosol Deposition Inside a Spent Fuel Transportation and Storage Canister*," SAND2021-5202R.

Sparrow, E. M. and A. L. Loeffler (1959). "Longitudinal Flow Between Cylinders arranged in a Rectangular Array," *American Institute of Chemical Engineers Journal* **5** (3) 325-330.

Tamayol, A. and M. Bahrami (2009). "Analytical Determination of Viscous Permeability of Fibrous Porous Media," *International Journal of Heat and Mass Transfer* **52**, 2407-2414.

Tamayol, A. and M. Bahrami (2010). "Parallel Flow Through Ordered Fibers: An Analytical Approach," *Journal of Fluids Engineering* 132, 114502. (2010, November 3). doi:https://doi-org.srv-proxy2.library.tamu.edu/10.1115/1.4002169.

The OpenFOAM Foundation. (n.d.). C++ Source Code Guide. (doxygen) Retrieved July 7, 2021, from https://cpp.openfoam.org/v3/a01946.html#details.

Westinghouse. (n.d.). *Westinghouse Technology Systems Manual; Technical Training Center*, Chattanooga, Tennessee.

Zigh, G. and S. Gonzalez, "Validation of Computational Fluid Dynamics Methods Using Prototypic Light Water Reactor Spent Fuel Assembly Thermal-Hydraulic Data," NUREG-2208, 2017.

This page left blank.

Appendix A. Geometric Parameters

Table 7. Fuel assembly basket geometric parameters.

Parameter	Value inch (mm)	Source
Basket width	8.86 (255.04)	*Westinghouse Technology Systems Manual;Technical Training Center Chattanooga, Tennessee.* (Westinghouse)
Basket height	173.5 (4406.9)	NAC, PDF pages 191/786 and 201/786
Assembly height	151.6 (3851)	*Westinghouse Technology Systems Manual;Technical Training Center Chattanooga, Tennessee.* (Westinghouse), Figure 3.1-20
Fuel pin outer diameter	0.374 (9.50)	*Westinghouse Technology Systems Manual;Technical Training Center Chattanooga, Tennessee.* (Westinghouse), page 3.1-26
Fuel pin spacing	0.496 (12.60)	*Westinghouse Technology Systems Manual;Technical Training Center Chattanooga, Tennessee.* (Westinghouse), Figure 3.1
Number of pins	264 fuel pins 25 guide/instrument tubes	*Westinghouse Technology Systems Manual;Technical Training Center Chattanooga, Tennessee.* (Westinghouse), page 3.1-26 (17×17 PWR assembly)
Guide/instrument cylinder outer diameter	0.482 (12.2)	*Westinghouse Technology Systems Manual;Technical Training Center Chattanooga, Tennessee.* (Westinghouse), page 3.1-26
Basket cross-sectional area	78.50 in^2 (50645 mm^2)	Square of basket inner square dimension $(8.86)^2$ in^2
Porosity	0.572	$1 - \frac{\pi}{basket\ cross-sect\ area}$ $\left[\left(\frac{pin\ diameter}{2}\right)^2 (264) + \left(\frac{guide\ diameter}{2}\right)^2 (25)\right]$

Appendix B. GCI Study

The grid convergence index (GCI) is designed to give a measure of the discretization error present in a computational model. A full description of the GCI method can be found at the NASA Glenn Research Center website (National Aeronautics and Space Administration, 2021). Essentially, the results of the model for three different mesh nodalizations with increasing refinement are compared to estimate the model error. This requires that the results of all three computations be close enough to the true value that the result asymptotically approaches the true value. The results of the three computations are sufficient to calculate the model's order of convergence using the following expression,

$$p = \frac{ln\left(\frac{\epsilon_{12}}{\epsilon_{23}}\right)}{ln(r)} \tag{14}$$

where
p = the order of convergence,
r = the grid refinement ratio, and
ϵ_{ij} = the relative error between each pair of grids.

The relative error is calculated between each pair of computations with (15) and (16)

$$\epsilon_{12} = \frac{f_2 - f_1}{f_1} \tag{15}$$

$$\epsilon_{23} = \frac{f_3 - f_2}{f_2} \tag{16}$$

where
f_i = the result from each grid.

The grid refinement ratio, r, is determined by the ratio of grid sizes along each refinement direction. In cases such as this investigation, where each block is not perfectly rectangular, the refinement ratio can be calculated by

$$r = \left(\frac{N_1}{N_2}\right)^{\frac{1}{D}} \tag{17}$$

where
N_i = the number of finite volumes in each grid, and
D = the number of dimensions along which the grid is refined.

Finally, the GCI is calculated between each discretization size change from (18) and (19)

$$GCI_{12} = \frac{F_s|\epsilon_{12}|}{(r^p - 1)} \tag{18}$$

$$GCI_{23} = \frac{F_s|\epsilon_{23}|}{(r^p - 1)} \tag{19}$$

where
F_s = a safety factor of 1.25 for three-grid GCI studies.

GCI_{12} is taken to be the estimated discretization error for the model. GCI_{23} is useful in verifying the three computational results are asymptotically approaching the true value. If the results are indeed asymptotically approaching the true value, the ratio $\frac{GCI_{23}}{GCI_{12} * r^p}$ should be equal to 1.0.

The grids chosen for this GCI are shown in **Error! Reference source not found.**, and correspond to a refinement ratio of 1.5, along with the resultant permeability constant, K. These computations were completed using a pressure drop of 10 psi and a fluid dynamic viscosity of 4.0×10^{-6} Pa*s.

Table 8. Summary of results from GCI study.

Grid Number	Number of finite volumes	Permeability (m^2)
1	9,052,160	1.873×10^{-6}
2	30,551,040	1.862×10^{-6}
3	103,109,760	1.858×10^{-6}

From the results presented in Table 8, the order of convergence for this model was determined to be 1.506. GCI_{12} is 0.108%, and GCI_{23} is 0.342%. Checking for the asymptotic region yields a ratio $\frac{GCI_{23}}{GCI_{12} * r^p}$ of 0.998, which is very close to 1.0. Visually, Figure 18 shows how the results of each case asymptotically approach some value as the number of cells used is increased. Therefore, each of the three grids is within the asymptotic region. Based on these results, the estimated discretization error for this model is $\pm$ 0.11%.

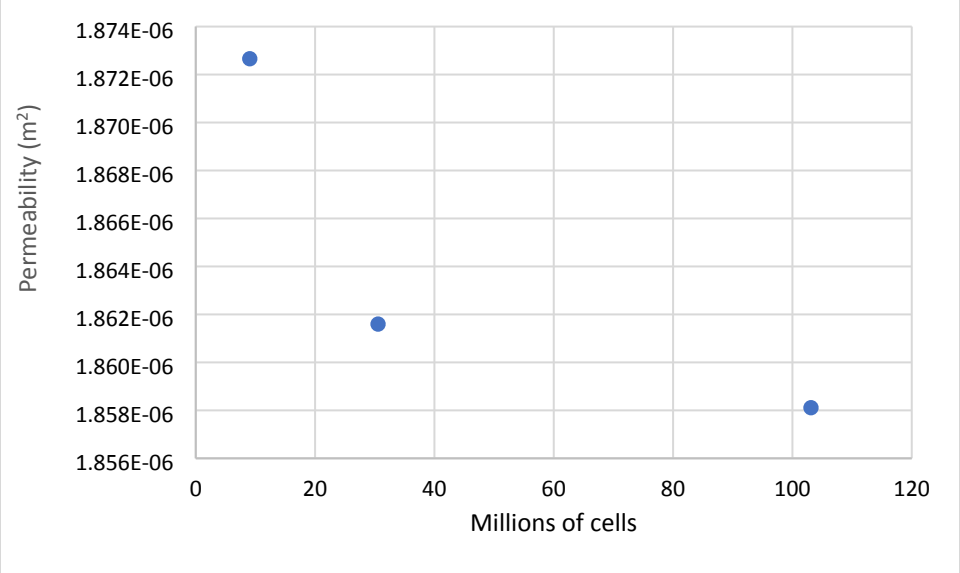

Figure 18. Plot of permeability as a function of cell count.

This page left blank.

Distribution

Email—Internal

Name	Org.	Sandia Email Address
Sylvia Saltzstein	8840	sisaltz@sandia.gov
Samuel Durbin	8843	sdurbin@sandia.gov
Geoff Freeze	8843	gafreez@sandia.gov
Eric Lindgren	8843	erlindg@sandia.gov
Laura Price	8843	llprice@sandia.gov
Fred Gelbard	8852	fgelbar@sandia.gov
Dallin Keesling	8852	dkeesli@sandia.gov
David Luxat	8852	dlluxat@sandia.gov
Jesse Phillips	8852	jphill@sandia.gov
Technical Library	01977	sanddocs@sandia.gov

Email—External

Name	Email Address	Affiliation
Prof. K. V. Kirtland	vierow@tamu.edu	Texas A&M University

This page left blank

This page left blank

Sandia National Laboratories

Sandia National Laboratories is a multimission laboratory managed and operated by National Technology & Engineering Solutions of Sandia LLC, a wholly owned subsidiary of Honeywell International Inc. for the U.S. Department of Energy's National Nuclear Security Administration under contract DE-NA0003525.